Monthly Notices
of the
ROYAL ASTRONOMICAL SOCIETY

MNRAS **438,** 2898–2915 (2014)
Advance Access publication 2014 January 13

doi:10.1093/mnras/stt2398

CO(1–0) survey of high-z radio galaxies: alignment of molecular halo gas with distant radio sources★

B. H. C. Emonts,[1,2]† R. P. Norris,[2] I. Feain,[3] M. Y. Mao,[4] R. D. Ekers,[2] G. Miley,[5] N. Seymour,[2] H. J. A. Röttgering,[5] M. Villar-Martín,[1] E. M. Sadler,[3] C. L. Carilli,[4] E. K. Mahony,[6] C. de Breuck,[7] A. Stroe,[5] L. Pentericci,[8] G. A. van Moorsel,[4] G. Drouart,[7] R. J. Ivison,[9] T. R. Greve,[10] A. Humphrey,[11] D. Wylezalek[7] and C. N. Tadhunter[12]

[1]*Centro de Astrobiología (INTA-CSIC), Ctra de Torrejón a Ajalvir, km 4, E-28850 Torrejón de Ardoz, Madrid, Spain*
[2]*CSIRO Astronomy and Space Science, Australia Telescope National Facility, PO Box 76, Epping NSW 1710, Australia*
[3]*School of Physics, University of Sydney, NSW 2006, Australia*
[4]*National Radio Astronomy Observatory, PO Box 0, Socorro, NM 87801-0387, USA*
[5]*Leiden Observatory, University of Leiden, PO Box 9513, NL-2300 RA Leiden, the Netherlands*
[6]*Netherlands Institute for Radio Astronomy, Postbus 2, NL-7990 AA Dwingeloo, the Netherlands*
[7]*European Southern Observatory, Karl Schwarzschild Strasse 2, D-85748 Garching, Germany*
[8]*INAF Osservatorio Astronomico di Roma, Via Frascati 33, I-00040 Monteporzio (RM), Italy*
[9]*Institute for Astronomy, University of Edinburgh, Blackford Hill, Edinburgh EH9 3HJ, UK*
[10]*Department of Physics and Astronomy, University College London, Gower Street, London WC1E 6BT, UK*
[11]*Centro de Astrofísica da Universidade do Porto, Rua das Estrelas, P-4150-762 Porto, Portugal*
[12]*Department of Physics and Astronomy, University of Sheffield, Sheffield S3 7RH, UK*

Accepted 2013 December 11. Received 2013 November 15; in original form 2013 July 18

ABSTRACT

We present a CO(1–0) survey for cold molecular gas in a representative sample of 13 high-z radio galaxies (HzRGs) at $1.4 < z < 2.8$, using the Australia Telescope Compact Array. We detect CO(1–0) emission associated with five sources: MRC 0114-211, MRC 0152-209, MRC 0156-252, MRC 1138-262 and MRC 2048-272. The CO(1–0) luminosities are in the range $L'_{\rm CO} \sim (5–9) \times 10^{10}$ K km s^{-1} pc^2. For MRC 0152-209 and MRC 1138-262, part of the CO(1–0) emission coincides with the radio galaxy, while part is spread on scales of tens of kpc and likely associated with galaxy mergers. The molecular gas mass derived for these two systems is $M_{\rm H2} \sim 6 \times 10^{10}$ M$_\odot$ ($M_{\rm H2}/L'_{\rm CO} = 0.8$). For the remaining three CO-detected sources, the CO(1–0) emission is located in the halo (∼50-kpc) environment. These three HzRGs are among the fainter far-IR emitters in our sample, suggesting that similar reservoirs of cold molecular halo gas may have been missed in earlier studies due to pre-selection of IR-bright sources. In all three cases, the CO(1–0) is aligned along the radio axis and found beyond the brightest radio hotspot, in a region devoid of 4.5 μm emission in *Spitzer* imaging. The CO(1–0) profiles are broad, with velocity widths of ∼1000–3600 km s^{-1}. We discuss several possible scenarios to explain these halo reservoirs of CO(1–0). Following these results, we complement our CO(1–0) study with detections of extended CO from the literature and find at marginal statistical significance (95 per cent level) that CO in HzRGs is preferentially aligned towards the radio jet axis. For the eight sources in which we do not detect CO(1–0), we set realistic upper limits of $L'_{\rm CO} \sim 3–4 \times 10^{10}$ K km s^{-1} pc^2. Our survey reveals a CO(1–0) detection rate of 38 per cent, allowing us to compare the CO(1–0) content of HzRGs with that of other types of high-z galaxies.

Key words: galaxies: active – galaxies: evolution – galaxies: haloes – galaxies: high-redshift – galaxies: jets – radio lines: galaxies.

★ Based on Australia Telescope Compact Array observations.

† E-mail: bjornemonts@gmail.com

1 INTRODUCTION

High-redshift radio galaxies (HzRGs, with $L_{500\,MHz} > 10^{27}$ W Hz^{-1}) are among the most massive and best-studied galaxies in the early Universe (Seymour et al. 2007; De Breuck et al. 2010). They have traditionally been identified by the ultrasteep spectrum of their easily detectable radio continuum, which served as a beacon for tracing the faint host galaxy environment (Röttgering et al. 1994; Chambers, Miley, van Breugel & Huang 1996). HzRGs have been observed to be the signposts of large overdensities in the early Universe, the so-called protoclusters that are believed to be the ancestors of local rich clusters (e.g. Venemans et al. 2007; Miley & De Breuck 2008; Wylezalek et al. 2013). The radio host galaxies are typically the massive central sources of these protoclusters and are surrounded by giant (100 kpc-scale) ionized gas haloes (Villar-Martín et al. 2002, 2003, 2006, 2007; Humphrey et al. 2007, 2013). A significant fraction of these gaseous emission-line haloes show spatially resolved absorption from extended regions of neutral gas (van Ojik et al. 1997a; Jarvis et al. 2003; Humphrey et al. 2008b).

HzRGs are in a very active stage of their evolution. They show clumpy optical morphologies (Pentericci et al. 2001), which indicates that continuous mergers are taking place. They often also contain evidence for massive star formation (e.g. Dunlop et al. 1994; Ivison 1995; Ivison et al. 2000; Archibald et al. 2001; Stevens et al. 2003; Barthel et al. 2012; Seymour et al. 2012; Rocca-Volmerange et al. 2013). Alignments have been seen between the radio synchrotron jets that emanate from the central supermassive black hole and optical/UV emission from warm gas and stellar continuum (e.g. Chambers, Miley & van Breugel 1987; McCarthy et al. 1987), as well as X-ray emission (e.g. Carilli et al. 2002; Smail & Blundell 2013) and dust re-radiated submillimetre emission (Stevens et al. 2003). The powerful radio jets can also exert significant feedback on to the surrounding interstellar medium (ISM; e.g. Villar-Martín et al. 2003; Humphrey et al. 2006; Nesvadba et al. 2006; Ogle et al. 2012). On average, HzRGs with smaller jets show stronger jet–ISM interaction, more intense star formation and larger reservoirs of neutral gas (van Ojik et al. 1997b; Humphrey et al. 2006, 2011).

A crucial component in the research on high-z protocluster radio galaxies is the study of cold molecular gas, which is the raw ingredient for star formation (and potential fuel for the AGN). An excellent review on the research of cold gas in high-z galaxies is given by Carilli & Walter (2013). Because molecular hydrogen (H_2) has strongly forbidden transitions, it can only be detected directly when it is shock-heated to high ($T > 100$ K) temperatures. An excellent tracer for the cold component of molecular gas is carbon monoxide (CO), because it is the most abundant molecule after H_2 and its excitation to the various ^{12}CO(J, $J-1$) transitions occurs at low temperatures, through collisions with H_2 (even at modest densities; Solomon & Vanden Bout 2005).

In the 1990, the first surveys for CO in HzRGs (mainly using the higher J-transitions) did not find any cold molecular gas (Evans et al. 1996; van Ojik et al. 1997b). Subsequently, improvements in millimetre receivers brought interesting results on CO in individual HzRGs between $z \sim 2$ and 5. (Scoville et al. 1997; Alloin et al. 2000; Papadopoulos et al. 2000, 2001, 2005; De Breuck et al. 2003a,b, 2005; Greve et al. 2004; Klamer et al. 2005; Ivison et al. 2008, 2012; Nesvadba et al. 2009; Emonts et al. 2011b, 2013, see also review by Miley & De Breuck 2008). In some cases CO is resolved on tens of kpc scales (Ivison et al. 2012), associated with various components (e.g. merging gas-rich galaxies; De Breuck et al. 2005; Emonts et al. 2013), or found in giant Lyα haloes that surrounds the host galaxy (Nesvadba et al. 2009). Several studies also identified alignments between the CO emission and the radio jet axis (Klamer et al. 2004; Nesvadba et al. 2009). These results show that detectable amounts of cold molecular gas in HzRGs are not restricted to the central region of the radio galaxy.

Despite these interesting results, a lack of sensitivity and bandwidth coverage at existing millimetre facilities (often not more than the width of the CO line, or the accuracy of the redshift) severely hindered systematic searches for molecular gas in HzRGs. Instead, targets were generally pre-selected on a high infrared (IR) of submillimetre (submm) luminosity.

The introduction of broad-bandwidth receivers at most of the large millimetre observatories has opened new possibilities for accurate searches for CO at high-z. A crucial species for quantifying the cold molecular gas is the ground transition CO(1–0). While the high-CO transitions trace dense and thermally excited gas in the central starburst/AGN region, only the lowest CO transitions may fully reveal widely distributed reservoirs of less dense, subthermally excited gas (e.g. Papadopoulos et al. 2000, 2001; Carilli et al. 2010; Ivison et al. 2011). The ground transition CO(1–0) is least affected by the excitation conditions of the gas; hence, observations of CO(1–0) provide the most robust estimates of the overall molecular gas content.[1] For high-z systems, observations of CO(1–0) require observing capabilities in the 20–50 GHz regime; hence, accurate studies of CO(1–0) at $z > 1.3$ have become feasible with the vastly improved millimetre receivers of the Karl G. Jansky Very Large Array and Australia Telescope Compact Array (ATCA; e.g. Aravena et al. 2010; Emonts et al. 2011a). Only a handful of observations of CO(1–0) in HzRGs currently exist, but they show evidence for large gas reservoirs (in some cases spread across tens of kpc; Emonts et al. 2011b, 2013; Ivison et al. 2012).

In this paper, we present a survey for CO(1–0) emission in a representative sample of 13 high-z radio galaxies with the ATCA. Throughout this paper, we will assume $H_0 = 71$ km s^{-1} Mpc^{-1}, $\Omega_M = 0.27$ and $\Omega_\Lambda = 0.73$.

1.1 Sample

We initially selected those HzRGs from the flux-limited 408 MHz Molonglo Reference Catalogue (Large et al. 1981) which were defined by McCarthy et al. (1996) to have $S_{408\,MHz} > 0.95$ Jy, $-30^\circ <$ Dec. $< -20^\circ$ and $9^h20^m <$ RA $< 14^h4^m$ or $20^h20^m <$ RA $< 6^h14^m$.[2] We subsequently selected for observing those sources for which the CO(1–0) line ($\nu_{rest} = 115.271\,203$ GHz) is observable in the ATCA 7 mm band (30–50 GHz), corresponding to a redshift range of $1.3 < z_{CO(1-0)} < 2.8$. In addition, in order to keep the sample manageable (given the large amount of observing time required; Section 2) and to maximize the scientific output, we only included sources for which complementary optical and IR data from the *Hubble Space Telescope* (*HST*) and *Spitzer* Space Telescope are available (Pentericci et al. 2001; Seymour et al. 2007; De Breuck et al. 2010). The well-studied source MRC 0211-112 (outside the declination range sampled by McCarthy et al. 1996) was also added to our sample (van Ojik et al. 1997a; Pentericci et al. 2001; Vernet et al. 2001; De Breuck et al. 2010; Humphrey et al. 2013).

[1] Although see Papadopoulos et al. (2012) for important caveats when using only CO(1–0) to determine the molecular gas content.

[2] This approach primarily selects sources based on their flux density, not their ultrasteep spectrum, as in other effective searches for HzRGs (Röttgering et al. 1994; Chambers et al. 1996).

Table 1. Observing details. z and $\nu_{CO(1-0)}$ are the redshift and central frequency at which we centred our '0'-velocity; t_{int} is the total on-source integration time; the last column lists the various calibrators that were used.

Name	z	$\nu_{CO(1-0)}$ (GHz)	Observing dates	t_{int} (h)	Calibrators (P = phase, B = bandpass, F = flux)
MRC 0114-211	1.402	47.998	03,09,22-AUG-11, 25,27-SEP-11, 23,24-OCT-11	24.8	0130-171 (P+B), 1921-293 (B), Uranus (F)
MRC 0152-209	1.9212	39.476	25,26-AUG-10, 28,29-SEP-10[a]	15.5	0130-171 (P+B), Uranus (F)
MRC 0156-252	2.016	38.220	05,07-AUG-10, 29-SEP-12	13.5	0135-247 (P+B), Uranus (F)
MRC 0211-122	2.340	34.512	08,10-AUG-11, 26,27-SEP-11	10.9	0202-172 (P+B), 0537-441 (B), Uranus (F)
MRC 0324-228	1.898	39.776	30-SEP-11, 20,21,22-OCT-11	11.1	0346-279 (P), 0537-441 (B), 1921-293 (B), 2223-052 (B), Uranus (F)
MRC 0350-279	1.900	39.749	30-SEP-11, 20,21,22-OCT-11	10.7	0346-279 (P), 0537-441 (B), 1921-293 (B), 2223-052 (B), Uranus (F)
MRC 0406-244	2.440	33.509	21,22-AUG-11, 15,16-SEP-11	14.0	0346-279 (P), 0537-441 (B), Uranus (F)
MRC 1017-220	1.768	41.644	24-OCT-11, 30,31-MAR-12, 25,26,27-SEP-12	17.2	1034-293 (P+B), Uranus (F) Mars (F)
MRC 1138-262	2.161	36.467	18,19-AUG-11, 26,27-SEP-11 13,14,15,16,17-MAR-12	22.0	1124-186 (P+B), Mars (F)
MRC 2025-218	2.630	31.755	12,13,14,15-AUG-10	17.4	1958-179 (P+B), 2008-159 (P+B), 1934-638 (F)
MRC 2048-272	2.060	37.670	21,22-AUG-11, 23-SEP-11 25-MAR-13, 03,04,05-OCT-13	19.8	2058-297 (P), 0537-411 (B), 1921-293 (B) 2223-052 (B), Uranus (F), G309 (F)
MRC 2104-242	2.491	33.020	18,19,20-SEP-09, 21,23-JUL-09	19.5	2008-159 (P+B), 2128-123 (P+B), 2149-306 (P), 2223-052 (B), Uranus (F)
MRC 2224-273	1.678	43.044	20,25,26-SEP-10, 01,02-OCT-10	15.3	2255-282 (P+B), Uranus (F)

[a]Additional high-resolution ATCA data of MRC 0152-209 are presented in Emonts et al. (in preparation).

In total, our sample consists of 13 southern MRC sources (see Table 1). All 13 sources have a 3 GHz rest-frame radio luminosity of $L_{3\,GHz} > 10^{27.5}$ W Hz^{-1} and they sample the full range in mid-IR (5 μm rest-frame) luminosities found across a large sample of HzRGs by De Breuck et al. (2010). Our sources also sample the *K*-band magnitude range covered by De Breuck et al. (2010) for objects with $16 < \mathrm{mag}_K \leq 19$, but our sample does not include sources in their lowest mag_K bin ($19 < \mathrm{mag}_K \leq 20$). We argue that this is likely because of optical/near-IR (NIR) selection biases in the existing *HST*/Wide-Field Planetary Camera 2 (WFPC2) and *HST*/Near Infrared Camera and Multi-Object Spectrometer (NICMOS) studies on which we based our sample selection.

An additional source (MRC 0943-242; $z = 2.92$) was observed in CO(1–0) just beyond the nominal edge of the ATCA 7 mm band ($\nu_{CO} = 29.4$ GHz), where increased noise and low-level instrumental effects prevented us from reaching the same sensitivity as for the 13 sample sources presented in this paper. MRC 0943-242 is therefore excluded from this paper. Results of MRC 0943-242, including a tentative CO(1–0) detection in the halo of this HzRG, have been described in Emonts et al. (2011a).

2 OBSERVATIONS

CO(1–0) observations were performed with the ATCA during 2009–2013 in the most compact hybrid H75, H168 and H214 array configurations (which contain both an EW and NS spur and maximum baselines of 89, 192 and 247 m, respectively). The bulk of the observations were done during the night in the southern late-winter and early-spring (months of Aug, Sept, Oct). A summary of the observations is given in Table 1.

The Compact Array Broadband Backend (CABB) with 2 × 2 GHz receiver bands was used in its coarsest spectral resolution of 1 MHz per channel (Wilson et al. 2011). For an object at $z = 2$ at which the CO(1–0) emission line ($\nu_{rest} = 115.271$ GHz) is observed at $\nu_{obs} = 38.400$ GHz, this setup results in a velocity coverage of 16 000 km s^{-1} per 2 GHz band with 8 km s^{-1} maximum spectral resolution. During the early observing period of this project (immediately after the CABB upgrade in 2009), several corrupted correlator blocks caused a significant number of channels to drop out in the first part of each 2 GHz band. We therefore centred the bands such that the expected CO(1–0) signal would fall in the clean part of each band. During the later period this problem did not occur, and we centred each band around the redshift of the expected CO(1–0) line. For redundancy (in case of technical issues, which occurred more frequently in the months after the CABB upgrade), both 2 GHz bands were centred around the same frequency, but because the signal is not independent in the two bands, only a single band was used in the final analysis of each observation. To better handle potential bandpass or systematic effects, we frequently introduced a small offset (tens to hundreds of MHz) in the central frequency of the bands between runs on a particular target.

For data calibration, we followed the strategy described in Emonts et al. (2011a). The phases (and in many cases also the bandpass) were calibrated every 5–15 min with a short (∼2 min) scan on a nearby bright calibrator (Table 1). In case the flux of this calibrator was <1 Jy, or the calibrator was not suitable for bandpass calibration, a strong bandpass calibrator was observed at the start, middle and end of each run. Fluxes were calibrated using (in order of preference) Uranus, Mars, PKS 1934-638 or the ultracompact H II region G309 (for the latter, see Emonts et al. 2011a). While the accuracy of the relative flux calibration between runs of the same target was $\lesssim$5 per cent, the error in absolute flux calibration was ∼20 per cent, due to a small difference in the models for the various flux calibrators. We note, however, that the latter only introduces a scaling factor that depends on the used flux calibrator for a particular source.

For the data reduction and visualization, we used the software packages MIRIAD (Sault, Teuben & Wright 1995) and KARMA (Gooch 1996). All of the HzRGs in our sample were detected in the 115 GHz

Table 2. Observed CO(1–0) properties: 'Beam' is the beam-size of the observations (with PA the position angle); rms is the root-mean-square noise in mJy beam^{-1} per channel (no Hanning smooth applied); Δv is the channel width; FWZI is the full width at zero intensity of the CO(1–0) profile; $I_{\rm CO(1-0)}$ and $L'_{\rm CO(1-0)}$ are the CO(1–0) intensity and luminosity; $M_{\rm H2}$ is the H_2 mass (see text for details); 'σ-level' is the significance level of the CO(1–0) signal integrated across its entire velocity range (see text for details).

Name MRC	Beam (PA) arcsec^2 (°)	rms (mJy beam^{-1})	Δv (km s^{-1})	FWZI (km s^{-1})	$I_{\rm CO(1-0)}$ (Jy beam^{-1} × km s^{-1})	$L'_{\rm CO(1-0)}$ (K km s^{-1} pc^2)	$M_{\rm H2}$ ($M_\odot$)	σ-level
0114-211	8.1 × 6.0 (89)	0.22	125	1130	0.43 ± 0.08	$4.5 \pm 0.9 \times 10^{10}$	$3.6 \pm 0.7 \times 10^{10}$	4.5σ
0152-209	9.8 × 7.1 (90)	0.23	40	800	0.37 ± 0.04	$6.6 \pm 0.8 \times 10^{10}$	$5.3 \pm 0.6 \times 10^{10}$	9σ
0156-252	6.9 × 4.9 (71)	0.17	154	2000	0.38 ± 0.09	$9.2 \pm 1.8 \times 10^{10}$	$7.4 \pm 1.5 \times 10^{10}$	5σ
0211-122	11.1 × 8.0 (99)	0.19	91	–	< 0.17	$< 4.6 \times 10^{10}$	$< 3.7 \times 10^{10}$	$<3\sigma$
0324-228	13.6 × 10.6 (106)	0.27	78	–	< 0.23	$< 4.2 \times 10^{10}$	$< 3.3 \times 10^{10}$	$<3\sigma$
0350-279	13.7 × 10.6 (102)	0.28	78	–	< 0.23	$< 4.3 \times 10^{10}$	$< 3.5 \times 10^{10}$	$<3\sigma$
0406-244	12.4 × 8.9 (77)	0.14	95	–	< 0.13	$< 3.7 \times 10^{10}$	$< 3.0 \times 10^{10}$	$<3\sigma$
1017-220	6.7 × 4.5 (84)	0.20	74	–	< 0.16	$< 2.6 \times 10^{10}$	$< 2.1 \times 10^{10}$	$<3\sigma$
1138-262	9.7 × 6.1 (66)	0.12	129	1680	0.31 ± 0.06	$7.2 \pm 1.3 \times 10^{10}$	$5.8 \pm 1.0 \times 10^{10}$	8σ
2025-218	7.8 × 4.8 (71)	0.16	94	–	< 0.15	$< 4.8 \times 10^{10}$	$< 3.8 \times 10^{10}$	$<3\sigma$
2048-272	7.1 × 5.2 (89)	0.10	210	3570	0.40 ± 0.09	$8.6 \pm 1.8 \times 10^{10}$	$6.9 \pm 1.5 \times 10^{10}$	5σ
(A)				(1260)	(0.21 ± 0.05)	(4.5 ± 1.1)	(3.6 ± 0.9)	(3.5σ)
(B)				(1260)	(0.19 ± 0.05)	(4.1 ± 1.1)	(3.3 ± 0.9)	(3.5σ)
2104-242	11.7 × 7.6 (97)	0.15	101	–	< 0.14	$< 2.7 \times 10^{10}$	$< 2.1 \times 10^{10}$	$<3\sigma$
2224-273	11.9 × 10.0 (93)	0.19	72	–	< 0.15	$< 2.2 \times 10^{10}$	$< 1.8 \times 10^{10}$	$<3\sigma$

rest-frame radio continuum at the mJy level. The continuum was separated from the line data by fitting a straight line to the line-free channels in the uv-domain. Because of the large velocity coverage per 2 GHz receiver band, the continuum subtraction could initially be done reliably using all channels, without affecting a potential weak CO signal. For those cases where CO(1–0) was detected, the continuum subtraction was repeated by excluding the channels in which the faint CO(1–0) signal was present. We note, however, that this did not significantly alter the final results. For MRC 0114-211, the radio continuum flux is ∼80 mJy. This allowed us to do a self-calibration on the continuum of MRC 0114-211, whose solutions were copied to the corresponding line data. The velocity axis of each individual line data set was transformed into optical barycentric velocity definition with respect to the redshift of the object (as given in Table 1). While each data set was reduced and analysed individually for CO signals, as well as for spurious signals or abnormalities, a Fourier transform was eventually performed on the combined line data for each object in our sample, using robust +1 weighting (Briggs 1995). Because of the low peak-flux of our CO(1–0) detections, no cleaning was done on the line data, except for a mild cleaning of the strong CO(1–0) signal in MRC 0152-209 (Section 3). The line data were subsequently binned to the results given in Table 2 and Figs 1 and 2. Total intensity images were made by summing the signal across the channels in which CO(1–0) was detected (without setting a noise threshold/cutoff). Values of $L'_{\rm CO(1-0)}$ from the CO(1–0) detections provided in this paper have been derived from these total intensity images. The beam-size and rms noise level of our data is summarized in Table 2. The primary beam of our observations is 80 arcsec at $\nu_{\rm obs} = 35$ GHz.

The continuum data for each object were combined into a map of the 115 GHz rest-frame emission. By comparing the location of the peak emission (and in some cases also the morphological structure) of this radio continuum with published high-resolution 4.7 and 8.2 GHz data (Carilli et al. 1997; Pentericci et al. 2000a; De Breuck et al. 2010), we were able to verify that the positional accuracy of our mm data (line and continuum) is better than 1 arcsec. The presentation of the continuum data is left for a future paper.

3 RESULTS

3.1 CO detections and upper limits

We detect CO(1–0) emission associated with five of our sample sources. These are MRC 0114-211 ($z = 1.40$), MRC 0152-209 ($z = 1.92$), MRC 0156-252 ($z = 2.02$), MRC 1138-262 (also called the 'Spiderweb Galaxy'; $z = 2.16$) and MRC 2048-272 ($z = 2.06$). The CO(1–0) emission-line profiles of these five sources are shown in Fig. 1 and their properties are summarized in Table 2. The characteristics and spatial distribution of the CO(1–0) emission in these sources will be discussed in Section 3.2.

The CO(1–0) emission-line luminosities of the five CO(1–0) detected sources in Fig. 1 are in the range $L'_{\rm CO} = 4.5$–9.2×10^{10} K kms^{-1} pc^2 (see Table 2). $L'_{\rm CO}$ was calculated following Solomon & Vanden Bout (2005, and references therein):

$$L'_{\rm CO} = 3.25 \times 10^7 \left(\frac{\int_{\rm v} S_{\rm CO}\delta v}{\rm Jy\,km\,s^{-1}}\right) \left(\frac{D_{\rm L}}{\rm Mpc}\right)^2 \left(\frac{\nu_{\rm rest}}{\rm GHz}\right)^{-2} (1+z)^{-1}, \quad (1)$$

with $\int_{\rm v} S_{\rm CO}\delta v = I_{\rm CO}$ the integrated flux density of the CO(1–0) emission and $L'_{\rm CO}$ expressed in K kms^{-1} pc^2.

Uncertainties in $L'_{\rm CO}$ are calculated following Sage (1990), assuming that they are dominated by the noise in the spectrum:

$$\Delta I_{\rm CO} = \sigma \Delta v \sqrt{\frac{\rm FWZI}{\Delta v}} (\rightarrow \text{uncertainty in } L'_{\rm CO}) \quad (2)$$

with σ the root-mean-square (rms) noise, Δv the channel width and FWZI (full width at zero intensity) the full width over which the CO profile was integrated. A second error term in $\Delta I_{\rm CO}$ arises from an uncertainty in determining the baseline ($\Delta I_{\rm CO}^{\rm baseline} = \sigma \Delta v_{\rm co} \sqrt{\Delta v_{\rm c}/\Delta v_{\rm b}}$, with $\Delta v_{\rm co}$ the FWZI of the CO signal, $\Delta v_{\rm c}$ the channel width and $\Delta v_{\rm b}$ the length of the baseline; see Sage 1990). However, because of the large CABB bandwidth ($\Delta v_{\rm baseline} \gg \Delta v_{\rm channel}$), this term is expected to be negligible. Our quoted uncertainties in $L'_{\rm CO}$ do not include the 20 per cent uncertainty in absolute flux calibration (Section 2).

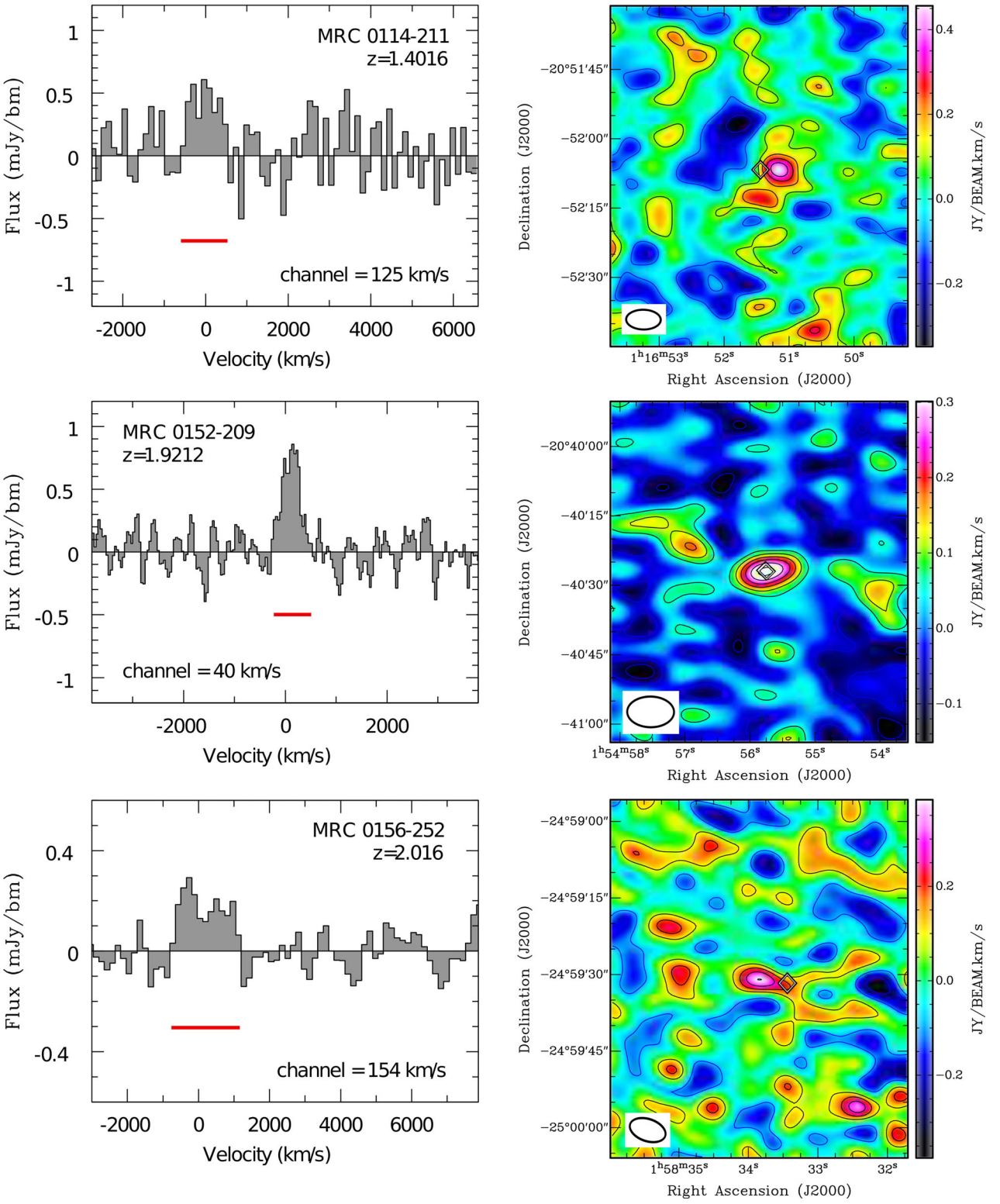

Figure 1. CO(1–0) spectra and total intensity images of the five CO-detected sample sources: MRC 0114-211, MRC 0152-209 (Emonts et al. 2011b), MRC 0156-252, MRC 1138-262 (Emonts et al. 2013) and MRC 2048-272. The channel width of the plotted spectra is shown at the bottom of each plot and was chosen to best visualize the CO(1–0) detection. For MRC 0152-209, MRC 0156-252 and MRC 1138-262 a Hanning-smoothed version of the spectra is shown to best visualize the CO(1–0) emission, while for MRC 0114-211 and MRC 2048-272 no Hanning smoothing was applied to better distinguish the CO(1–0) emission from the noise characteristics across the bandpass. The 0-velocity is defined as the optical redshift of the host galaxy (see De Breuck et al. 2000, and references therein), except for MRC 0114-211, where the uncertainty in optical redshift is as large as the velocity coverage of our CO observations (see Appendix A). The red bar indicates the velocity range across which we integrated to obtain the total intensity map of each source. Contours levels are spaced 1σ apart (with $\sigma = 0.094$, 0.095, 0.095, 0.046, 0.080 Jy beam^{-1} $\times$ km s^{-1} for MRC 0114-211, MRC 0152-209, MRC 0156-252, MRC 1138-262, MRC 2048-272, respectively). The diamond indicates the position of the host galaxy.

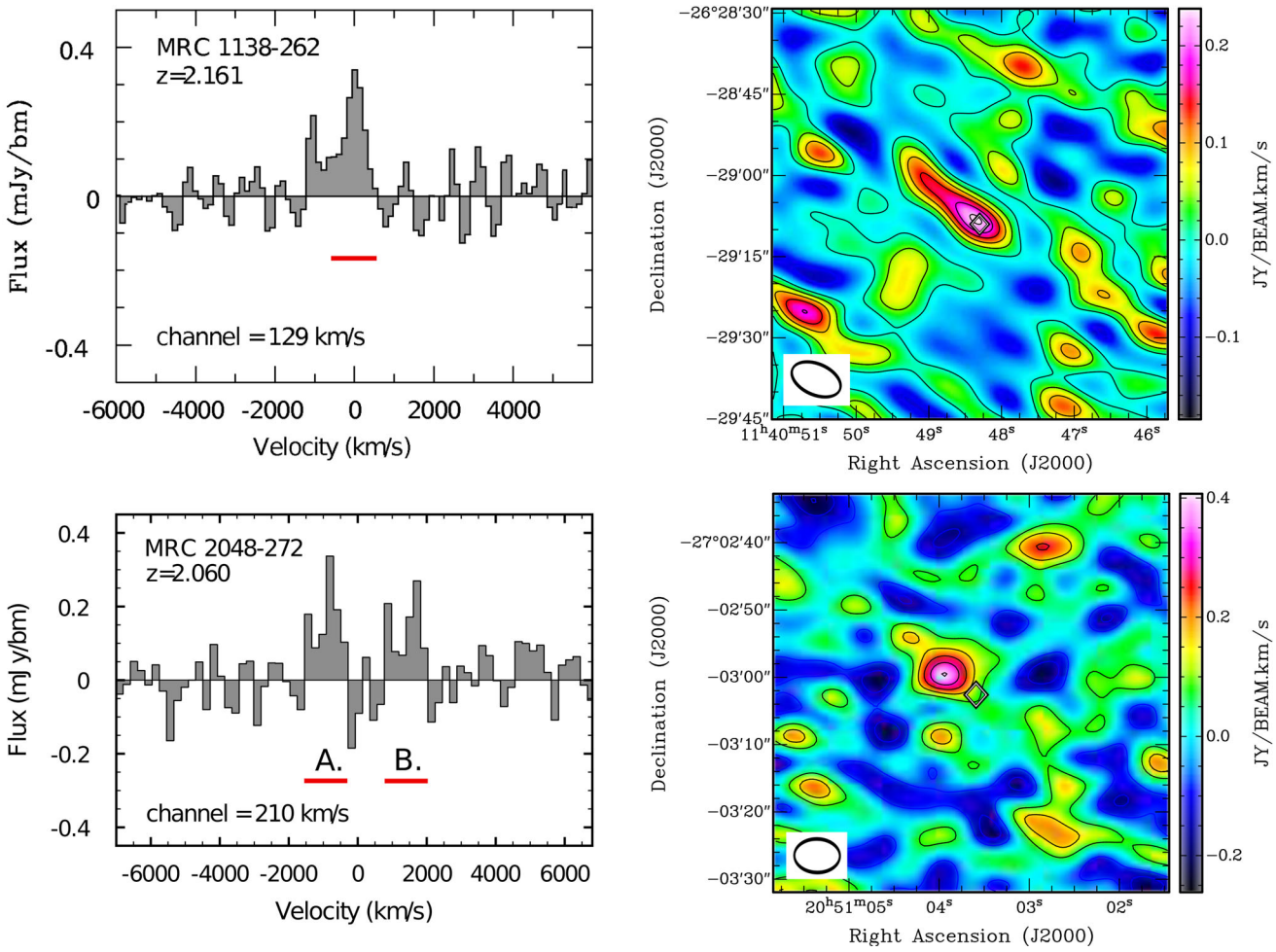

Figure 1 – *continued*

To derive realistic upper limits for the non-detections in our sample, we set boundary conditions based on the CO(1–0) characteristics of our five CO-detected sources. They show CO(1–0) components with FWZI = 800−2000 km s^{-1}. In addition, the widest profiles (MRC 0156-252, MRC 1138-262 and MRC 2048-272) appear to be double-peaked and cannot be fitted with a single-Gaussian profile. This makes any assumption on the shape of the expected profile for the non-detections unjustified. We therefore derive conservative upper limits on $L'_{\rm CO}$ for the non-detected HzRGs in our sample by assuming a 3σ signal smoothed across 1000 km s^{-1} (FWZI):

$$I_{\rm CO} < 3\sigma\,\Delta v\sqrt{\frac{1000}{\Delta v}}\;\left(\rightarrow \text{ upper limits } L'_{\rm CO}\right). \qquad (3)$$

Results are given in Fig. 2 and Table 2.

3.1.1 *Significance level of the CO(1–0) detections*

An important consideration in the interpretation of our results is the significance of the CO(1–0) signals that we detect. In Table 2, we show the signal-to-noise level of the *integrated* CO(1–0) signal.[3]

Most of the CO(1–0) detections presented in this paper are found $\lesssim$1 synthesized beam-size from the core of the radio galaxy (Section 3.2) and near the redshift determined from optical emission-line observations (De Breuck et al. 2000, and references therein), resulting in a low probability that these signals are spurious (see Krips, Neri & Cox 2012). For sources that showed an initial tentative CO(1–0) signal (including MRC 0114-211, MRC 0156-252 and MRC 2048-272), we continued observing them until the tentative CO(1–0) signal was either confirmed or judged spurious. The two main criteria that we used for confirming a CO(1–0) signal are (1) indications for the CO(1–0) emission are present across the different observing runs; (2) at a channel-binning that is optimized to reveal the integrated CO(1–0) signal, the CO(1–0) emission stands out above the noise as the signal with the highest absolute value across the full primary beam and frequency coverage of the data cube. All five CO-detected sources in our sample satisfy these criteria. Appendix A provides additional details on our five CO(1–0) detections.

Krips et al. (2012) show that blind CO searches (i.e. searches for CO emission not associated with objects with known coordinates

[3] For MRC 1138-262 (Fig. 3), MRC 0152-209 (Fig. 4) and MRC 0156-252 (Fig. 7), the CO(1–0) signal could be separated into distinct kinematic components that peak at a different spatial location. In these cases, we derive the significance level of the 'integrated' CO(1–0) profile as $\sqrt{\sum (s_c{}^2)}$, with s_c the σ-level of the different kinematic components. These values are somewhat higher than those shown in Fig. 1, because one avoids adding noise from regions in which no CO(1–0) emission is found.

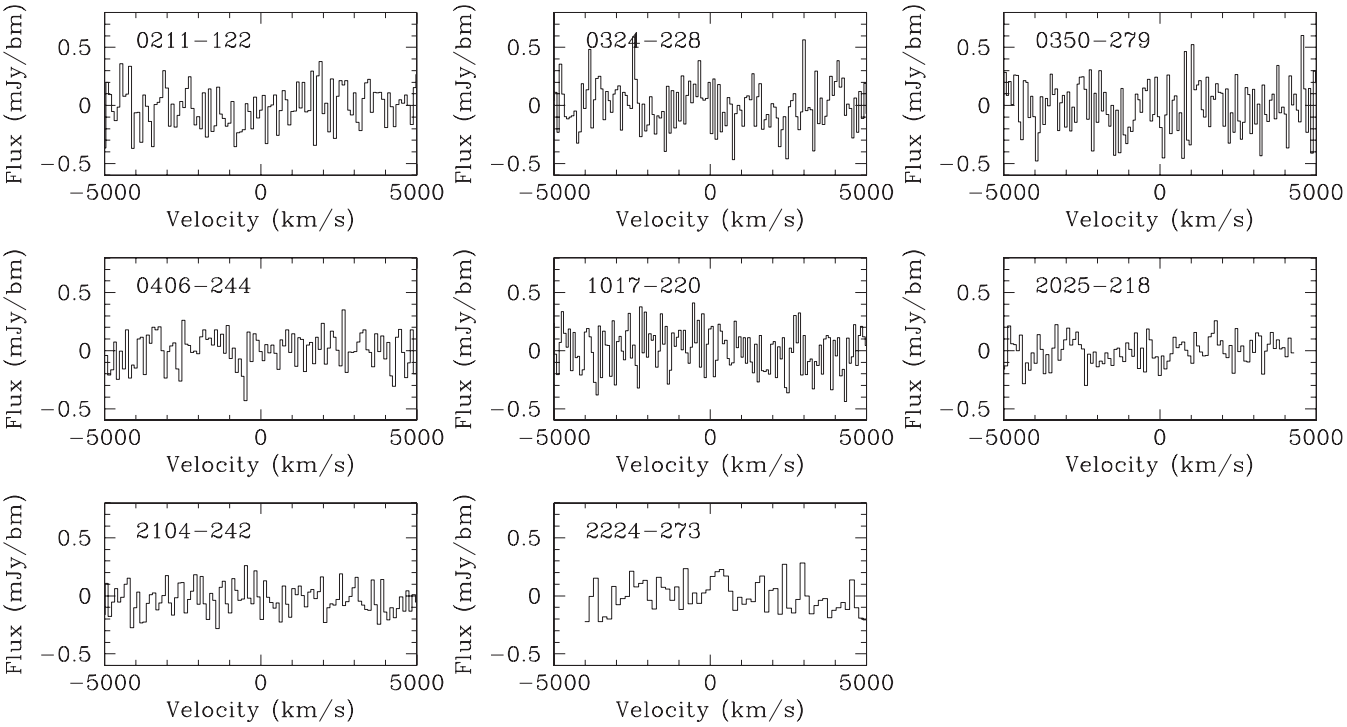

Figure 2. Spectra of the sample sources that were not detection in CO(1–0). The spectra were binned by 10 channels to velocity resolutions of roughly 100 km s^{-1} (see Section 2 and Table 2). The spectrum of MRC 2224-273 (last window) was binned by 20 channels to visualize a low-level feature around the redshift of the object (which significance is too low to claim a detection).

and redshifts) are likely to result in spurious CO detections at a 5σ level (see also Aravena et al. 2012). Because many of the HzRGs in our sample have no, or no complete, information on protocluster galaxies in their environment, and because our observing strategy was not optimized for a blind CO(1–0) search, this paper does not address the CO(1–0) content of the larger (hundreds of kpc) environment of these HzRGs.

3.2 CO characteristics

In this section we briefly discuss the characteristics of the CO(1–0) detections across our sample. Details on the individual sources are given in Appendix A.

3.2.1 'On-source' CO(1–0) emission

For two of the five CO(1–0) detected sources (MRC 0152-209 and MRC 1138-262), a substantial fraction of the CO(1–0) emission coincides with the bright optical/NIR emission associated with the radio galaxy. In both cases, however, part of the CO(1–0) emission is also spread across scales of several tens of kpc (Figs 3 and 4). This is consistent with the idea that observations of the ground-transition CO(1–0) are sensitive to tracing wide-spread cold molecular gas (Papadopoulos et al. 2001, see also Section, 1). Results on MRC 0152-209 and MRC 1138-262 are presented in detail in related papers (Emonts et al. 2011b, 2013; Emonts et al., in preparation), and will thus only be briefly summarized here.

Fig. 3 shows the CO(1–0) distribution in MRC 1138-262 (from Emonts et al. 2013).[4] As discussed in Emonts et al. (2013), the kinematics of the CO(1–0) emission appears to follow the velocity distribution of several satellite galaxies in the same region; hence, the extended part of the CO(1–0) is likely associated with (interacting/merging) satellites or the intergalactic medium (IGM) between them.

Fig. 4 shows high-resolution ATCA data of MRC 0152-209 (Emonts et al., in preparation), which is a follow-up study of our original low-resolution work (Emonts et al. 2011b). MRC 0152-209 is a gas-rich major merger system at $z = 2$, with a double nucleus and prominent tidal tails in *HST*/NICMOS and WFPC2 imaging (Pentericci et al. 2001; Emonts et al., in preparation). While the bulk of the CO(1–0) emission is co-spatial with the main body of the host galaxy, part of it seems to follow the optical tidal features. Interestingly, the small radio source appears to be aligned with the NW component of the off-nuclear CO(1–0) emission.

Galaxy mergers and interactions thus seem important to explain the CO(1–0) distribution in both MRC 0152-209 and MRC 1138-262. This is consistent with the suggestions by Ivison et al. (2012) that galaxy mergers are ubiquitous among starburst radio galaxies at high-z.

3.2.2 'Off-source' CO(1–0) emission

For the remaining three CO-detected sources in our sample (MRC 0114-211, MRC 0156-252 and MRC 2048-272), the CO(1–0) emission is offset from the radio galaxy. As can be seen in Fig. 5, for all three sources *the CO(1–0) emission is located along the*

[4] Fig. 3 only includes the CO(1–0) features from Emonts et al. (2013) that have recently been confirmed with additional ATCA observations (Emonts et al., in preparation). Several additional 3σ features of the original data presented in Emonts et al. (2013) have not yet been confirmed due to poor weather conditions during the new observations, and hence, they are not included in Fig. 3.

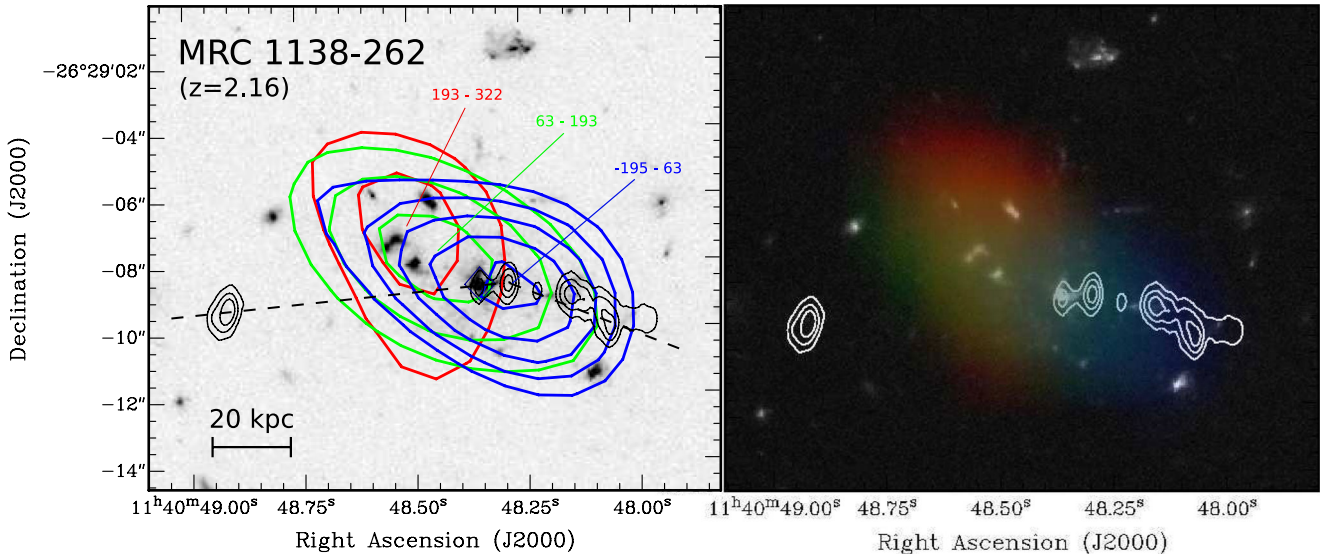

Figure 3. Spatial distribution of the CO(1–0) emission associated with MRC 1138-262 (see also Emonts et al. 2013). *Left*: CO(1–0) emission integrated over three distinct velocity ranges and overlaid on to an *HST*/ACS image from Miley et al. (2006). The velocity ranges for the three components are indicated in the plot (in km s^{-1}). A velocity gradient is visible in the CO(1–0) emission, which is spread across scales of 30–40 kpc (see Emonts et al. 2013 for details, including channel maps and spectra). CO(1–0) contour levels are at 3, 3.8, 4.6, 5.4, 6.2σ level (with $\sigma = 0.033$ Jy beam^{-1} $\times$ km s^{-1} for the red/green components and 0.047 Jy beam^{-1} $\times$ km s^{-1} for the blue component). The beam-size of the ATCA data is 9.7 arcsec $\times$ 6.1 arcsec (PA = 66°). The thin black contours show the 8.2 GHz radio continuum image from Carilli et al. (1997), while the black dotted line visualizes the extrapolated radio jet axis. *Right*: three-colour image of the CO(1–0) components from the left plot overlaid on to the *HST* image.

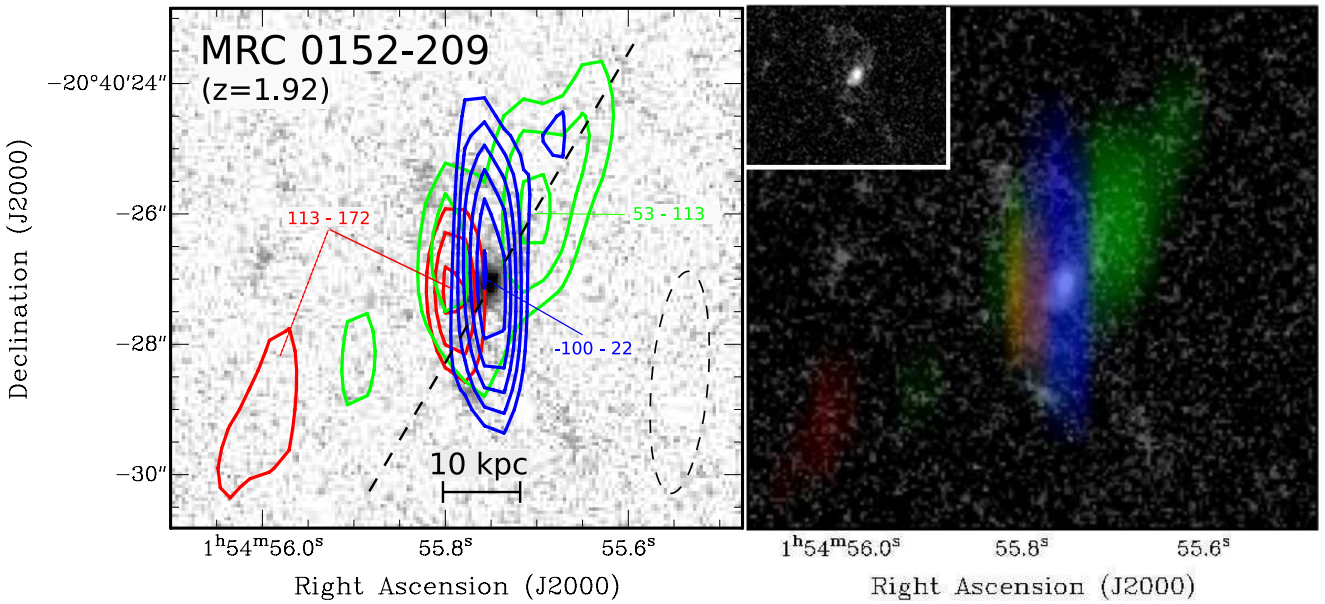

Figure 4. Spatial distribution of the CO(1–0) emission associated with MRC 0152-209 (see Emonts et al., in preparation for details, including channel maps and spectra; see Emonts et al. 2011b for the original CO(1–0) detection). *Left*: CO(1–0) emission integrated over three distinct velocity ranges and overlaid on to an *HST*/WFPC2$_{F555W}$ [Programme 8183; PI: Miley] image (Emonts et al., in preparation). The velocity ranges for the three components are indicated in the plot (in km s^{-1}). CO(1–0) contour levels are at 2.8, 3.5, 4.2, 4.9, 5.6σ level (with $\sigma = 0.0073$ Jy beam^{-1} $\times$ km s^{-1} for the red/green components and 0.012 Jy beam^{-1} $\times$ km s^{-1} for the blue component). Note the highly elongated beam (dashed ellipse) that we obtained by using the extended-baseline east-west array configurations of the ATCA, which resulted in a lack of uv-coverage in north–south direction by staying above the typical 30° elevation suitable for millimetre observations (see Emonts et al., in preparation for details). The radio source (not shown in this plot) has a total linear extent of only 2.2 arcsec (18 kpc; Pentericci et al. 2000b), while the black dotted line visualizes the extrapolated radio jet axis. *Right*: three-colour image of the CO(1–0) components from the left-hand plot overlaid on to the *HST* image. The inset in the top-left highlights the prominent optical tidal features.

radio axis, on the side of the brightest radio emission, and found beyond the outer radio hotspot. The alignment of the CO with the radio jet axis is within 20° for the three sources. A fourth case may be the NW 'off-source' component of CO(1–0) emission in MRC 0152-209 (Section 3.2.1 and Fig. 4), as it shows a similar alignment with the small radio jet. These alignments resemble earlier results by Klamer et al. (2004) and Nesvadba et al. (2009). It suggests that there is a causal connection between the propagating

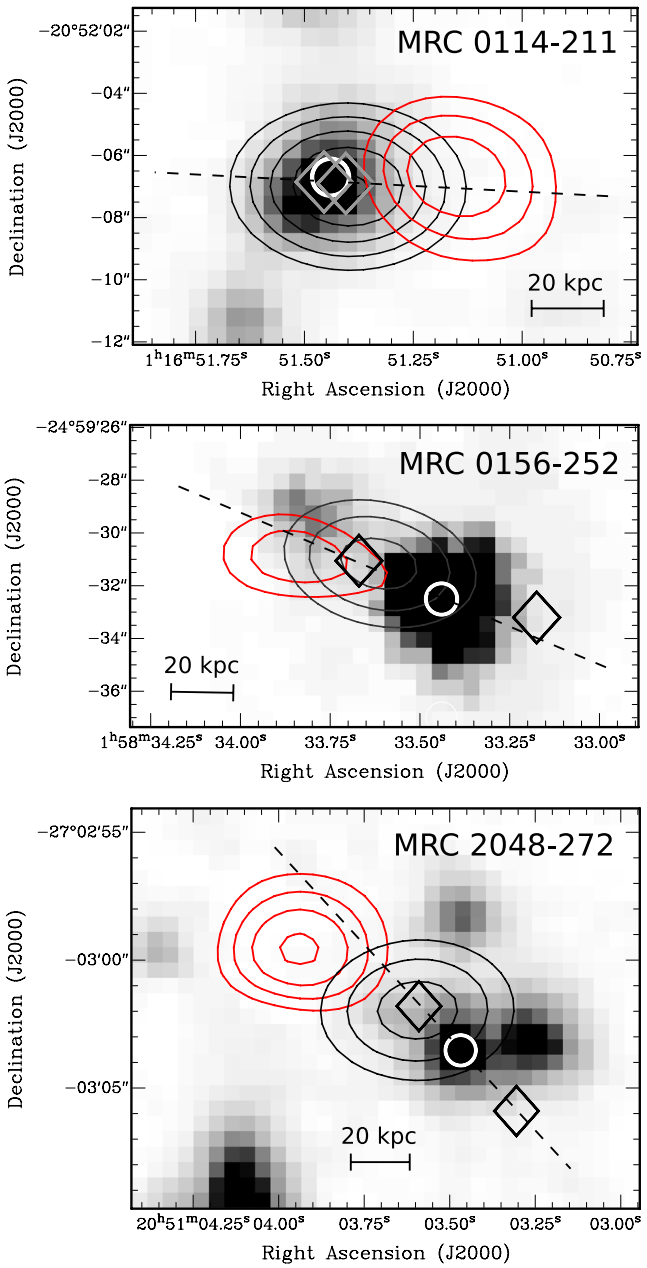

Figure 5. Spatial distribution of the CO(1–0) emission associated with MRC 0114-211, MRC 0156-252 and MRC 2048-272. The red contours show the CO(1–0) emission at 2.8, 3.5, 4.2, 4.9σ level (with σ = 0.094, 0.095 and 0.080 Jy beam^{-1} × km s^{-1} for MRC 0114-211, MRC 0156-252 and MRC 2048-272, respectively). The black contours represent the 7 mm radio continuum (levels: 42, 52, 62, 72, 82 mJy beam^{-1} for MRC 0144-211; 6, 8, 10 mJy beam^{-1} for MRC 0156-252 and 1.6, 2.2, 2.8 mJy beam^{-1} for MRC 2048-272). The radio continuum and CO(1–0) emission were obtained from the same data set, so their relative astrometry is accurate. The lowest radio contour was chosen to represent the beam-size of the observations. The background plots are *Spitzer*/IRAC 4.5 μm images from Wylezalek et al. (2013) and Galametz et al. (2012). The white circle shows the location of the radio galaxy from *HST*/NICMOS imaging (Pentericci et al. 2001), while the diamonds indicate the location of the radio hotspots in high-resolution radio imaging (ν_{obs} = 8 GHz; Pentericci et al. 2001; De Breuck et al. 2010). The dotted line visualizes the extrapolated radio jet axis.

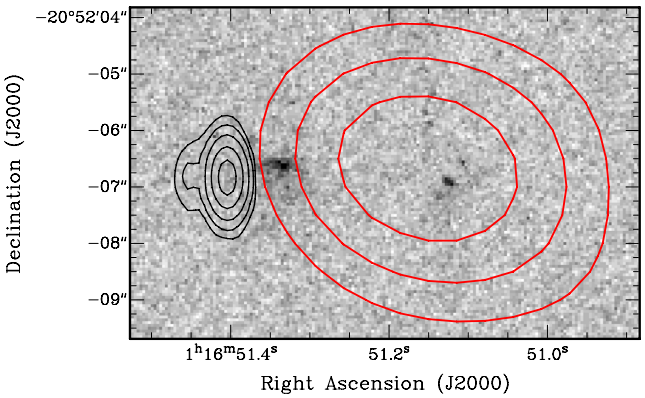

Figure 6. *HST*/WFPC2$_{F555W}$ image of the region around MRC 0114-211, overlaid with the contours of CO(1–0) emission (red) and 4.8 GHz radio continuum from De Breuck et al. (2010; black). Contour levels CO(1–0): 2.8, 3.5, 4.2σ (with σ = 0.094 Jy beam^{-1} × km s^{-1}). The accuracy of the *HST* astrometry has not been confirmed to better than ∼1.5 arcsec (see text).

radio jets and the presence of large amounts of cold molecular gas in the halo environment of these sources (which we will discuss further in Section 4.2).

The peak of the CO(1–0) emission is located at an apparent ∼10, 30 and 40 kpc distance from the radio hotspot for MRC 0156-252, MRC 0114-211 and MRC 2048-272, respectively. However, the synthesized beam-size of our data corresponds to 60–70 kpc at these redshifts, and undetectable lower surface brightness radio plasma may be present beyond the hotspot, so sensitive high-resolution CO observations and deeper low-frequency radio imaging are required to further investigate how close the cold gas is located to the radio source.

While L'_{CO} of these three off-nuclear CO-emitters is similar to what is found in submillimetre galaxies (SMGs; see Section 4.4), Fig. 5 shows that no *Spitzer*/IRAC 4.5 μm emission is found at the location of the CO(1–0) to a level of 1–2 mag below L^* (see Galametz et al. 2012; Wylezalek et al. 2013). For MRC 0114-211, however, the CO(1–0) emission is co-spatial with a very faint optical (i.e. near-UV rest-frame) counterpart that is visible in an archival *HST*/WFPC2$_{F555W}$ image (Fig. 6). Brighter optical emission is found just outside the edge of the bright western radio jet, reminiscent of a shell of shocked emission-line gas, such as the one that Overzier et al. (2005) found around the bended radio lobe in MRC 0156-252. It is possible, however, that the error in the astrometry of the archival *HST* image is as much as 1.5 arcsec (see Appendix A) and that the bright optical emission is the host galaxy.

Fig. 7 shows that the CO(1–0) emission in MRC 0156-252 is located just outside a large reservoir of Lyα emission, with the boundary region between the Lyα and CO(1–0) gas occurring at the edge of the radio hotspot. The CO(1–0) emission consists of two kinematically distinct peaks that both lie ∼20 kpc distance from two satellite galaxies detected with *HST*/NICMOS (Pentericci et al. 2001). The innermost companion (near the blue CO peak) has blue colours that are indicative of enhanced star formation (possibly triggered by the passage of the radio jet; Pentericci et al. 2001). Very recent work by Galametz et al. (2013) suggests that the redshift at which we centred the CO(1–0) profile (z = 2.016) is more closely related to the redshift of this blue companion than that of the HzRG (see Appendix A for details).

For MRC 2048-272, the two kinematically distinct CO(1–0) components from Fig. 1 peak at the same spatial location (see Appendix A for details).

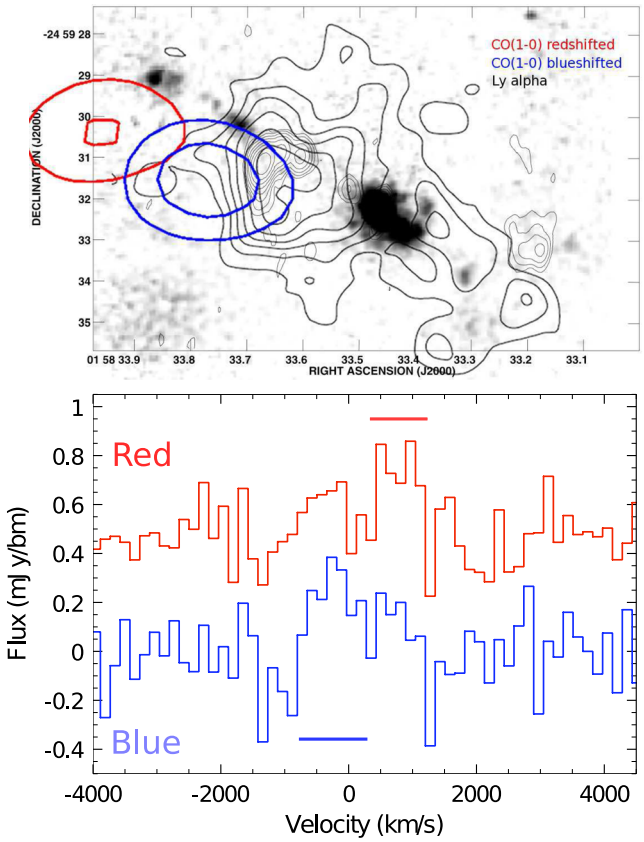

Figure 7. *Top*: spatial distribution of the CO(1–0) emission associated with MRC 0156-252. The blue and red contours are the blue- and redshifted part of the CO(1–0) profile from Fig. 1 (integrated over the velocity ranges −800–+275 and +275–+1200 km s^{-1}, respectively, as indicated by the bars in the bottom plot). Contour levels are at 2.8 and 3.5σ level (with $\sigma = 0.055$ and 0.064 Jy beam^{-1} × km s^{-1} for the red and blue component, respectively). The thick black contours are Lyα emission, the thin black contours 8.2 GHz radio continuum and the grey-scale *HST*/NICMOS imaging, all from Pentericci et al. (2001). *Bottom*: spectra at the location of the blue and red peak in the top plot. As can be seen, both spectra are not fully independent due to the large beam-size of our observations.

We also note that the CO(1–0) emission of these three off-nuclear detections covers a wide velocity range (1100 < FWZI < 3600 km s^{-1}). The CO(1–0) profiles are broad compared to what is generally found in quasars and SMGs (Coppin et al. 2008; Wang et al. 2010; Ivison et al. 2011; Riechers et al. 2011; Krips et al. 2012; Bothwell et al. 2013), with the exception of what is found in a few high-z merging galaxies (see Salomé et al. 2012, and references therein). Possible scenarios on the nature of the off-nuclear CO(1–0) emission in MRC 0114-211, MRC 0156-252 and MRC 2048-272 are discussed in Section 4.2.

3.3 Derivation of H_2 mass

Molecular gas masses (and upper limits) are estimated from L'_{CO} using a conversion factor $X_{CO} = M_{H2}/L'_{CO} = 0.8$ M$_\odot$ (K km s^{-1} pc^2)$^{-1}$ (where M_{H2} includes a helium fraction; e.g. Solomon & Vanden Bout 2005). This value is found for ultraluminous infrared galaxies ($L_{IR} > 10^{12}$L$_\odot$; Downes & Solomon 1998) and is within the range of $X_{CO} = 0.8$–1.6 M$_\odot$ (K km s^{-1} pc^2)$^{-1}$ assumed for high-z SMGs and star-forming galaxies (Stark et al. 2008; Tacconi et al. 2008). However, we stress that X_{CO} depends on important properties of the gas (such as metallicity, extinction and radiation field; Papadopoulos et al. 2008b; Glover & Mac Low 2011; Bolatto, Wolfire & Leroy 2013), and is not yet well understood (Tacconi et al. 2008; Ivison et al. 2011, see additional discussion in Section 4.2.2).

Taking the above into account, our assumed $X_{CO} = 0.8$ M$_\odot$ (K km s^{-1} pc^2)$^{-1}$ results in molecular gas mass estimates in the range $M_{H2} = 4$–7×10^{10} M$_\odot$ for the CO(1–0) detected HzRGs in our sample. Value and upper limits of M$_{H2}$ are given in Table 2.

4 DISCUSSION

We have performed a systematic search for CO(1–0) emission of cold molecular gas in a representative sample of 13 HzRGs and have presented five CO(1–0) detections. The most intriguing result from this work is that we find three cases where bright CO(1–0) emission is found along the radio jet axis and beyond the outer radio hotspot. This indicates that the alignments seen in HzRG between the radio jets and optical/UV (Chambers et al. 1987; McCarthy et al. 1987), X-ray (Carilli et al. 2002; Smail & Blundell 2013) and submm emission (Stevens et al. 2003) now also have to take into account the component of cold molecular CO(1–0) gas.

In Section 4.1, we will first present a comparison between $L'_{CO(1-0)}$ and the far-IR (FIR) luminosity (L_{FIR}) from the starburst component. We will use this information in Section 4.2 to interpret the alignments that we find between the radio source and cold molecular halo gas in several of our sample sources. A more statistical investigation of the radio–CO alignment, based on CO results from the literature, is given in Section 4.3. In Section 4.4, we will compare the CO(1–0) properties of HzRGs with those of other types of high-z galaxies.

4.1 Cold gas (L'_{CO}) versus starburst (L_{FIR})

Following the Schmidt–Kennicutt relation between star formation and gas reservoir (Schmidt 1959; Kennicutt 1998), relations between L'_{CO} and the FIR luminosity (L_{FIR}) are frequently observed in both low- and high-z galaxies (see Ivison et al. 2011; Villar-Martín et al. 2013, for recent examples). Fig. 8 shows L'_{CO} plotted against the starburst component of L_{FIR} for our sample sources. Values of $L_{FIR-starburst}$ (hereafter L_{FIR}) are from Drouart et al. (in preparation) and have been derived from modelling the overall spectral energy distribution across 8–1000 μm to separate the starburst from other, e.g. torus and stellar, components. Details and a list of L_{FIR} values will be provided in Drouart et al. (in preparation).

Given the small range of L'_{CO} and L_{FIR} values that our sample covers, it is not surprising that there is no clear trend visible. However, it is interesting that the sources in which we detect CO(1–0) solely offset from the central host galaxy (MRC 0114-211, MRC 0156-252 and MRC 2048-272) have a starburst FIR luminosity that falls in the lower half of the L_{FIR} values of our sample sources. This suggests that earlier studies that pre-selected targets based on their high FIR luminosity may have missed similar systems where detectable amounts of molecular gas are located outside the host galaxy, but in the galaxy's halo environment.

MRC 1138-262 and MRC 0152-209 (the two sample sources where part of the CO(1–0) emission coincides with the host galaxy) are among the stronger FIR emitters in the sample. Their high FIR luminosity implies high star formation rates (up to ∼1400 M$_\odot$ yr^{-1}; Emonts et al. 2011b; Seymour et al. 2012). As discussed in Emonts et al. (2011b, 2013), if the CO(1–0) represents a reservoir of molecular gas that is consumed by this massive star formation, the minimum gas depletion time-scale in these two HzRGs is of the order

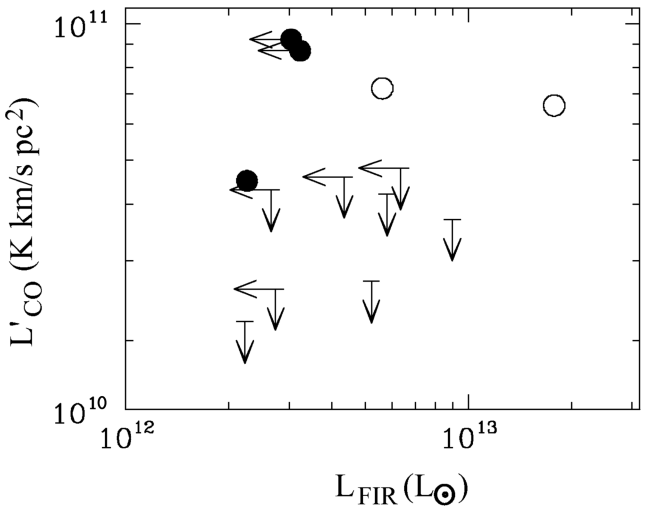

Figure 8. L'_{CO} plotted against the starburst FIR luminosity L_{FIR} (8–1000 μm). Values of L_{FIR} are from Drouart et al. (in preparation). The open circles represent MRC 0152-209 and MRC 1138-262, in which a large fraction of the CO(1–0) emission coincides with the central radio galaxy. The filled circles show the three sources where the CO(1–0) emission is solely detected offset from the radio galaxy.

of 40 Myr. This is comparable to the typical lifetime of a massive burst of star formation in ultraluminous IR ($L_{IR} > 10^{12}$ L$_\odot$) merger systems (e.g. Mihos & Hernquist 1994).

When comparing the CO(1–0) luminosity of our sample sources with other properties of the host galaxy (as observed by Pentericci et al. 2000a; De Breuck et al. 2010), we find no apparent correlation between L'_{CO} and z, $P_{500\,W\,Hz^{-1}}$, spectral index $\alpha^{4.7\,GHz}_{8.2\,GHz}$, total linear extent of the radio source and core fraction of 20 GHz radio continuum. Three of our CO(1–0) detected sources (MRC 1138-262, MRC 0156-252 and MRC 0152-209) appear to have a relatively high stellar mass (in the range 0.5–2 $\times$ 10^{12} M_*), compared to the CO non-detections ($M_* < 0.5 \times 10^{12}$ M$_\odot$; De Breuck et al. 2010). With better statistics it would be worth investigating whether there is a trend between $L'_{CO(1-0)}$ and M_*.

4.2 Cold halo gas: radio–CO alignment

Our survey suggests that CO reservoirs of cold molecular gas exist in the halo (∼50 kpc-scale) environment of a significant fraction of HzRGs. These cold gas reservoirs are likely part of metal-enriched quiescent Lyα haloes that have been observed to surround HzRGs (Villar-Martín et al. 2003, 2006, 2007; Binette et al. 2006). Extended reservoirs of neutral hydrogen gas and large dusty shells have also been observed in these Lyα haloes (van Ojik et al. 1997a; Jarvis et al. 2003; Humphrey et al. 2008b, 2013).

The most intriguing result from this paper is that this CO(1–0) is preferentially aligned along the radio jet axis and found beyond the brightest part of the radio continuum. This is similar to the case of TXS 0828+193 ($z = 2.6$), where Nesvadba et al. (2009) found CO(3–2) emission ($L'_{CO} \sim 2 \times 10^{10} \times$ K kms^{-1} pc^2) beyond the tip of the SW hotspot (∼80 kpc from the radio core). No optical or IR counterpart was detected at this location and the CO kinematics are in good agreement with those of C IV emission at the edge of the optical gaseous halo (Villar-Martín et al. 2002). Our results also resemble the radio−CO alignments found in $z >$ 3 radio galaxies by Klamer et al. (2004) as well as in the $z \sim 0.3$ quasars [H89]1821+643 (Blundell & Rawlings 2001; Aravena et al. 2011) and HE 0450-2958 (Feain et al. 2007; Papadopoulos et al. 2008b; Elbaz et al. 2009). We here address several possible explanations for this alignment.

4.2.1 *Jet-induced star formation or gas cooling*

Klamer et al. (2004) found that in $z > 3$ radio galaxies CO and dust emission are also preferentially aligned along the radio axis. They discuss a scenario in which the CO is formed in sites of star formation that are initially triggered by the radio jets – a mechanism that may perhaps also explain alignments found between the radio jets and UV/optical continuum (Chambers et al. 1987; McCarthy et al. 1987; Begelman & Cioffi 1989; De Young 1989; Rees 1989; Bicknell et al. 2000), or the increased star formation rates found in AGN with pronounced radio jets (Zinn et al. 2013). Klamer et al. (2004) make three predictions for the scenario of jet-induced star formation that our independent CO(1–0) results appear to confirm, namely that the CO in HzRGs is extended and aligned with observable synchrotron radio emission (see our Fig. 5), that the CO profiles from emission outside the host galaxy will be broad (see our Fig. 1) and that CO and Lyα emission will be tracing different physical regions (see our Fig. 7).

It is possible that at $z \sim 2$ (where the massive radio galaxies have already gone through several cycles of chemical enrichment) the CO is associated with jet-induced gas cooling that precedes the star formation, rather than being a product of the star formation itself. *Gas cooling* is feasible if the IGM is compressed and cooled through shocks induced by the radio source (e.g. Mellema, Kurk & Röttgering 2002; Sutherland, Bicknell & Dopita 2003; Fragile et al. 2004; Gaibler et al. 2012). As discussed in detail by Nesvadba et al. (2009), this may also result in cooling-flow processes similar to those observed in low-z giant central cluster galaxies (despite morphological and kinematical differences in the CO distribution, which in low-z cooling flows is mainly concentrated towards the central galaxy and along the sides of the cavities that are excavated by the radio lobes; e.g. Fabian 1994; Edge 2001; Salomé & Combes 2003; Salomé et al. 2006, 2011).

4.2.2 *Jet-driven enrichment*

An alternative scenario is that the carbon and oxygen were created during massive bursts of star formation within the host galaxy and subsequently transported into the halo environment by the radio source, forming a reservoir of metal-enriched gas beyond the edge of the radio plasma.

Jet-driven outflows of ionized, neutral and molecular gas have been observed along the radio axis in both low- and high-z radio galaxies (e.g. Morganti et al. 2003, 2005; Villar-Martín et al. 2003; Emonts et al. 2005; Humphrey et al. 2006; Holt, Tadhunter & Morganti 2008; Nesvadba et al. 2008; Dasyra & Combes 2012; Mahony et al. 2013; Morganti et al. 2013a,b). In addition, it is believed that powerful radio-loud AGN are responsible for the formation of filamentary extended emission-line regions in quasars (Fu & Stockton 2007a,b, 2009). Several studies suggest that the radio jets may also be responsible for transporting dust and metals far outside the host galaxy. In low-z brightest clusters galaxies, Kirkpatrick et al. (2009) and Kirkpatrick, McNamara & Cavagnolo (2011) find that metal-enrichment takes place along the radio axis. They show that heavy elements are often found beyond the extent of the innermost X-ray cavities, which suggests that the metal-enrichment by the radio source is sustained over multiple generations of radio outbursts. At high-z, Ivison et al. (2012) argue that jet-induced feedback

may explain a large (∼500 kpc) dusty filamentary structure that is co-aligned with the radio source 6C 1909+72 ($z = 3.5$).

Interestingly, extended emission-line haloes around HzRGs and quasars have been found to display near-solar metallicities (e.g. Vernet et al. 2001; Humphrey et al. 2008a; Prochaska & Hennawi 2009). It is interesting to speculate that in this metal-rich halo environment, the potentially low gas densities and high velocity dispersion of the cold gas (as traced by the wide FWZI of our CO profiles), in combination with a potentially high-pressure environment induced by the radio plasma and the absence of a strong stellar radiation field, may conspire in favour of a lower conversion factor than our assumed $X_{\rm CO} = 0.8$ (see Papadopoulos et al. 2008b; Glover & Mac Low 2011). This would lower the mass of molecular gas responsible for the bright CO(1–0) emission and alleviate the problem that this cold halo gas is found in regions devoid of *Spitzer* 4.5 μm emission. Because the CO(1–0) emission in the halo is produced in a profoundly different environment than models on the $X_{\rm CO}$ factor generally assume, a more detailed analysis of this is beyond the scope of this paper.

When considering the time-scales involved, assuming that the enriched material is expelled with a typical velocity of ∼500 km s^{-1} (Nesvadba et al. 2008), it would take the gas $\sim 6 \times 10^7$ yr to reach a distance of 30 kpc. In agreement, the typical lifetime of extended radio sources is expected to be at least several $\times\ 10^{7-8}$ yr (Parma et al. 1999; Blundell & Rawlings 2000). Overzier et al. (2005) argue that the nuclear activity in MRC 2048-272 has recently ceased (given the lack of X-ray and radio continuum in the core), indicating that this system is at the end of its current radio-loud AGN cycle.

In addition, in several $\times 10^7$ yr a major starburst episode may have passed its peak activity (e.g. Mihos & Hernquist 1994), which may perhaps explain why the hosts of the off-nuclear CO(1–0) emitters are fainter in the FIR than MRC 0152-209 and MRC 1138-262, which have the bulk of CO (still) centred on the host galaxy. While for MRC 0152-209 part of the CO(1–0) appears to extend along the radio axis (Section 3.2.1), it is also interesting to note that for MRC 1138-262 Nesvadba et al. (2006) detect a fast, redshifted ionized gas outflow along the same direction as the extended CO(1–0) emission (see Emonts et al. 2013 for a discussion).

If jet-driven enrichment is a viable scenario for the radio–CO alignment, we can make the testable predictions that (i) the chemical enrichment of the haloes around HzRGs should occur mainly along the radio jet axis, (ii) HzRGs with CO reservoirs in their haloes may have passed a peak-period of major starburst activity and (iii) there should be high-z galaxies in which the radio source has recently switched off (e.g. radio-quiet QSOs) with similar off-nuclear CO(1–0) reservoirs.

4.2.3 Jet-brightness enhancement by cold ISM

Alternatively, the CO(1–0) emission may represent tidal debris from the host or companion galaxies (similar to the tidal CO(1–0) gas we find around MRC 0152-209; Fig. 4), or a filamentary structure of cold molecular gas (possibly an imprint of the large-scale Cosmic Web in the centre of the protocluster; West, Villumsen & Dekel 1991; Springel, Frenk & White 2006; Ceverino, Dekel & Bournaud 2010). In those cases, the radio–CO alignment effect could occur because the working surface of the radio jet is brightest there where it encounters the densest medium (e.g. Barthel & Arnaud 1996). The characteristic bright radio continuum in HzRGs would then be a consequence of the fact that the synchrotron jets propagate into a high-density region. This scenario was also used by Stevens et al. (2003) to explain their observed alignment between the radio source and extended submm emission in and around HzRGs (and has also been invoked to explain the relatively high occurrence of bright, compact radio sources in gas-rich and starbursting radio galaxies at low-z; e.g. Morganti et al. 2011; Tadhunter et al. 2011; Emonts et al. 2012).

4.3 Radio–CO alignment: general statistics

As mentioned in Section 3.2, for all three HzRGs with CO(1–0) emission found solely at large distance from the host galaxy, the CO(1–0) emission is aligned to within 20° of the radio axis. For MRC 0152-209, the off-nuclear CO(1–0) emission towards the NE also appears to be aligned with the small radio jet (Section 3.2.1). The chance of CO(1–0) being aligned within 20° for four out of the five CO-detected sources in our sample is $\lesssim$1 per cent. However, the beam-size of our observations is large and these CO(1–0) signals peak at only $\sim 5\sigma$ significance, introducing substantial uncertainty in the exact location of the CO(1–0) emission. Moreover, given the low number of CO-detected sources in our sample, we cannot place reliable statistical significance on these results.

In order to investigate in a more statistical way whether there is evidence for a general alignment between CO emission and radio jets in HzRGs, we show in Table 3 and Fig. 9 a summary of all HzRGs (with $L_{500\,\rm MHz} > 10^{27}$ W Hz^{-1}) from the literature for which extended CO and radio emission have been imaged. We use a one-tailed Mann–Whitney U-test to verify the hypothesis that the CO emission in this sample is preferentially aligned towards the radio jet axis, compared to samples of equal size where the differences in position angle between the CO and radio are presented by randomly chosen numbers between 0° and 90°. We find marginal statistical significance at the 95 per cent level that such an alignment is present in the data.

These results are a largely independent confirmation of the results by Klamer et al. (2004), who derived their conclusions from a sample of high-z radio sources with a lower average radio power. We note, however, that we are still dealing with low-number statistics and that most of the studies from the literature where done with higher order CO transitions (which likely trace a different component of the gas than CO(1–0); Section 1). Larger samples observed with the Atacama Large Millimeter/submillimeter Array (ALMA) and the Karl G. Jansky Very Large Array (JVLA) are required to verify the alignment effect for various J-transitions of CO.

4.4 The CO(1–0) content of HzRGs

We detect CO(1–0) emission (with $L'_{\rm CO} > 4 \times 10^{10}$ L$_\odot$) associated with 38 per cent of our sample of southern HzRGs. In earlier studies, van Ojik et al. (1997b) did not detect any CO among a sample of 14 northern HzRGs (see also Evans et al. 1996). van Ojik et al. (1997b) derived upper limits of $L'_{\rm CO} \sim$ few $\times\ 10^{10}$ K km s^{-1} pc^2, but mainly using the higher order J-transitions. These high-J transitions are believed to trace the denser and often thermally excited gas in the more centrally concentrated starburst/AGN regions. Our results that the CO(1–0) emission in HzRGs is often spread across tens of kpc scales thus strengthen the idea discussed in Section 1 that studies of low- and high-J transitions may be biased towards tracing different reservoirs of molecular gas. Thus, while a direct comparison between our study and the earlier work by van Ojik et al. (1997b) and Evans et al. (1996) is difficult, it shows the need for sensitive studies of HzRGs across a wide range of molecular transitions and species.

Table 3. Literature study on the potential alignment of CO(J, $J-1$) emission with radio source axis in HzRGs. PA_{CO} and PA_R are the position angle of the CO emission and the radio jet (on the side where the CO emission occurs). $\psi = |PA_{CO} - PA_R|$ is the difference in position angle between the CO and radio jet. D_{CO} and D_R are the maximum distance out to which the CO and radio emission are detected. $R = D_{CO}/D_R$ is the ratio of these values, which thus gives an indication how far inside ($R < 1$) or outside ($R > 1$) the radio jet the CO emission is found.

Name	z	CO transition	PA_{CO} (°)	PA_R (°)	ψ (°)	D_{CO} (kpc)	D_R (kpc)	R (D_{CO}/D_R)	Refs.
4C 41.17	3.792	(4–3)	−140	−130	10	10.9	57.9	0.19	1,2
4C 60.07	3.791	(4–3)	−70	−123	53	43.4	45.6	0.95	3,4,5
6C 1908+7220	3.537	(4–3)	−127	−154	27	37.1	50.5	0.73	6,7
B3 J2330+3927	3.086	(1–0)/(4–3)	−154	−213	59	33.4	15.5	2.15	8,9
TXS 0828+193	2.6	(3–2)	−131	−141	10	78.0	56.9	1.37	2,10
MRC 1138-262	2.161	(1–0)	56	95	39	25.2	63.8	0.39	11
MRC 0156-252	2.016	(1–0)	76	67	9	59.3	25.4	2.33	11
MRC 2048-272	2.060	(1–0)	58	43	15	55.8	22.8	2.45	11
MRC 0152-209	1.921	(1–0)	−31	−32	1	25.5	18	1.42	11
MRC 0114-211	1.402	(1–0)	−92	−93	1	34.9	4.3	8.12	11

References. 1. De Breuck et al. (2005); 2. Carilli, Owen & Harris (1994); 3. Papadopoulos et al. (2000); 4. Ivison et al. (2008); 5. Carilli et al. (1997); 6. Pentericci et al. (2001); 7. De Breuck et al. (2003a); 8. Ivison et al. (2012); 9. Pérez-Torres & De Breuck (2005); 10. Nesvadba et al. (2009); 11. this work.

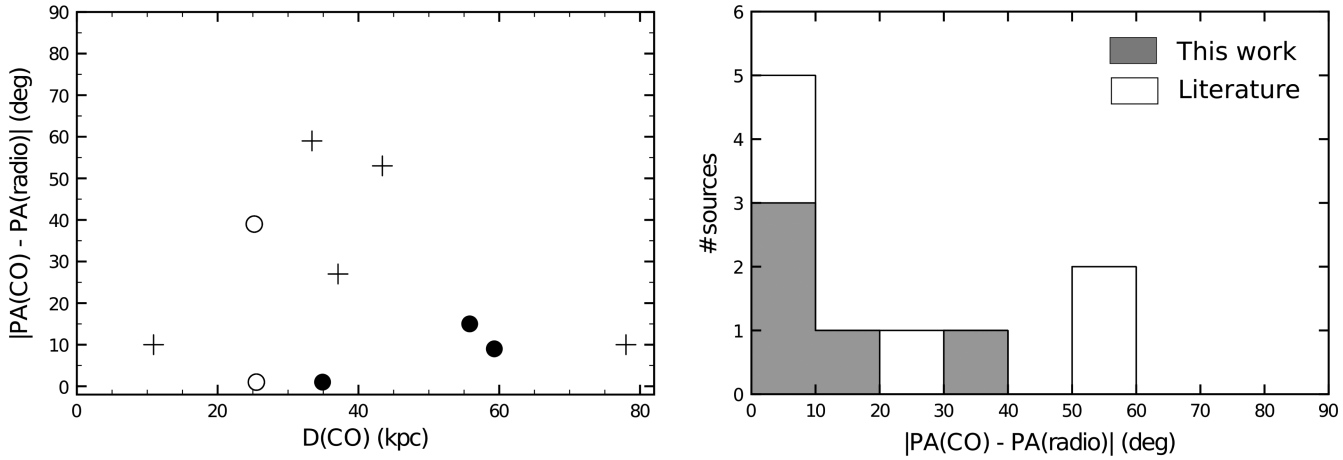

Figure 9. *Left*: difference in position angle (ψ) between the CO and synchrotron radio emission in HzRG (Table 3) plotted against the distance to which the CO emission extends. The filled and open circles are the same as in Fig. 8 and represent our sample sources detected in CO(1–0). The crosses are HzRGs with extended CO(J, $J-1$) emission from the literature. *Right*: histogram of the distribution of ψ among HzRGs with extended CO(J, $J-1$) emission.

4.4.1 *Low-J transitions at high-z: a comparison*

Our survey is the first survey for the ground-transition CO(1–0) in a representative sample of HzRGs. With upgrades to wide-band receivers and observing capabilities below 50 GHz at the large millimetre facilities, a growing number of studies are targeting the low-order CO transitions in various samples of high-z galaxies. This allows a fair comparison of the cold molecular gas content of these various types of galaxies, without having to deal with uncertainty in the thermalization of the gas or the possibility of missing CO emission due to the very limited velocity coverage that plagued past studies (see Section 1).

In Fig. 10, we compare the CO(1–0) content of our HzRGs with that of samples of other types of galaxies in the same redshift range as our sample sources ($z \sim 1.5$–2.5). We only included studies performed with wide-band receivers (covering $\geq$2000 km s^{-1}) that targeted either the CO(1–0) or CO(2–1) transition, resulting in comparison samples of SMGs (Hainline et al. 2011; Ivison et al. 2011; Bothwell et al. 2013), star-forming galaxies (Daddi et al. 2008; Dannerbauer et al. 2009; Aravena et al. 2010, 2012) and two obscured (type-2) quasi-stellar objects (QSO2; Lacy et al. 2011). Low-order CO observations done with narrow-band receivers (e.g. Papadopoulos et al. 2001; Greve et al. 2004, 2005) or observations that targeted either systems at $z > 2.5$ (e.g. Klamer et al. 2005; Ivison et al. 2008, 2012; Coppin et al. 2010; Carilli et al. 2011; Wang et al. 2011; Huynh et al. 2013; Riechers et al. 2013) or lensed systems (e.g. Swinbank et al. 2010; Danielson et al. 2011; Riechers et al. 2011; Johansson et al. 2012; Aravena et al. 2013; Rawle et al. 2013) are excluded from our high-z comparison in order to introduce as little bias as possible.

Fig. 10 shows $L'_{CO(1-0)}$ plotted against the starburst FIR luminosity L_{FIR} for the various types of high-z galaxies.[5] It is immediately clear that the five CO-detected HzRGs in our sample have a CO(1–0)

[5] It is likely that L_{FIR} in some of the SMGs and QSO2 that we present is contaminated by an AGN-contribution (unlike for the HzRG, where the AGN contribution is separated from the starburst L_{FIR} values; Section 4.1). However, we argue that this will not likely alter the main conclusions that we derive in this section.

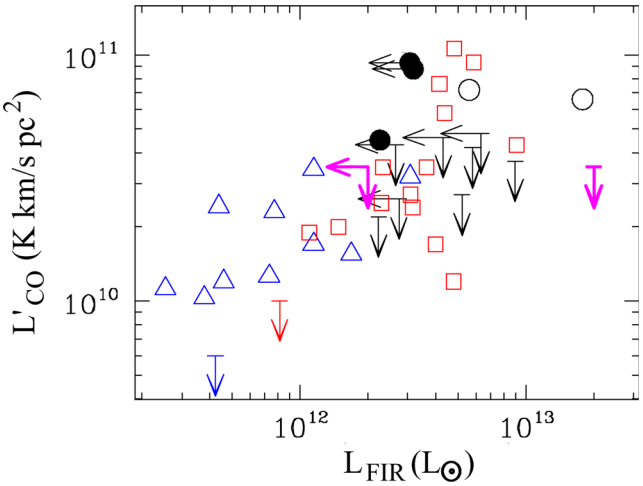

Figure 10. L'_{CO} plotted against the starburst FIR luminosity L_{FIR} for the various samples of high-z galaxies observed in CO(1–0) or CO(2–1). HzRGs (black symbols) are as in Fig. 8. Star-forming and 'BzK'-selected galaxies (blue triangles) are taken from Daddi et al. (2008) and Aravena et al. (2011, 2012) (see also Dannerbauer et al. 2009). SMGs (red squares + red arrow) are taken from Ivison et al. (2011) and Bothwell et al. (2013) (an SMG observed in CO(2–1) by Coppin et al. 2008 has been omitted due to a significant uncertainty in L_{FIR}). CO(1–0) upper limits on two obscured QSOs (magenta arrows) are taken from Lacy et al. (2011). For targets observed in CO(2–1), the ratio $L'_{CO(2-1)}/L'_{CO(1-0)}$ adopted by the original studies was used to transform to CO(1–0) values, though corrections are small.

luminosity that is comparable to what is found in the CO-brightest SMGs.

Our CO(1–0) detection rate of 38 per cent (taking into consideration a typical 3σ detection limit of $L'_{CO(1-0)} \lesssim 4 \times 10^{10}$ K km s^{-1} pc^2) is in rough agreement with the fact that 33 per cent of the SMGs observed in CO(1–0) or CO(2–1) have $L'_{CO(1-0)} \geq 4 \times 10^{10}$ K km s^{-1} pc^2 (Fig. 10). None of the $z \sim 1.5$–2.5 star-forming galaxies is detected in CO(1–0) at this level, which reflects in their lower L_{FIR}.

It is, however, interesting that when excluding the three off-nuclear CO(1–0) detections in our sample (i.e. when only taking into account CO detections at the location of the host galaxy), the CO(1–0) detection rate of HzRGs drops to less than half that of SMGs (assuming a similar sensitivity cutoff). It would be worth to verify a possible deficiency of CO(1–0) emission in HzRGs, and investigate whether this can be related to the observed shock-heating of molecular H_2 gas in the centres of HzRGs (Nesvadba et al. 2010; Guillard et al. 2012; Ogle et al. 2012) and the highly shock-excited ('above thermalization') CO-emitting gas found in some radio galaxies (Papadopoulos et al. 2008a; Ivison et al. 2012).

Larger CO surveys of unbiased samples with JVLA and ALMA are required to further investigate how the amount and properties of the CO-emitting gas in HzRGs compares to that of other types of high-z galaxies.

5 CONCLUSIONS

We have performed the first representative survey for cold molecular CO(1–0) gas in a sample of 13 HzRGs ($1.4 < z < 2.8$) using the ATCA. The main results from this work are:

(i) We detect CO(1–0) emission in 38 per cent (5/13) of our sample sources. The CO(1–0) luminosities are in the range $L'_{CO} = (4.5\text{–}9.2) \times 10^{10}$ K km s^{-1} pc^2, which correspond to molecular gas masses of $M_{H2} = (4\text{–}7) \times 10^{10}\,M_\odot$ when assuming $M_{H2}/L'_{CO} = 0.8$. The CO(1–0) profile for four of the five detections is broad (FWZI ∼1100–3600 km s^{-1}).

(ii) Only for two of these sources (MRC 0152-209 and MRC 1138-262), part of the CO(1–0) emission is co-spatial with the radio host galaxy, although a significant fraction of the CO(1–0) is spread across tens of kpc scales and likely related to the process of galaxy merging.

(iii) For the other three CO-detections (MRC 0114-211, MRC 0156-252 and MRC 2048-272), the CO(1–0) is found in the halo of the host galaxy. These three HzRG are among the fainter FIR emitters in the sample, indicating that large amounts of molecular halo gas ($L'_{CO(1-0)}$= several $\times 10^{10}$ K km s^{-1} pc^2) may have been missed in previous studies that mostly pre-selected targets based on a high FIR luminosity.

(iv) We find an alignment between the off-nuclear CO(1–0) emission and the radio jet axis, with the CO located outside the brightest edge of the radio source. We discuss several scenarios that may explain this, including jet-induced star formation/gas cooling, jet-driven metal-enrichment of the gaseous halo and flux boosting of jets that propagating into a dense filament of cold halo gas.

(v) Following our results, we performed a literature study on extended CO(J, $J-1$) emission in HzRG and find marginal statistical significance (95 per cent level) for the hypothesis that the CO is preferentially aligned towards to the radio axis.

(vi) The majority of the host galaxies of high-z radio sources does not contain CO(1–0) emission down to a secure limit of $L'_{CO} \sim 3\text{–}4 \times 10^{10}$ K km s^{-1} pc^2.

We have shown that from now on, the well-known alignments between the radio jets and optical, UV, X-ray and submm emission in HzRGs (see Section 1) will have to be discussed taking into account the component of cold molecular gas.

We note that the CO(1–0) emission that we found in the haloes of three HzRG may only reveal part of the cold molecular gas content around HzRGs, as our observations are only sensitive to tracing those sites where the CO emission is brightest. Follow-up observations with the ATCA, JVLA and ALMA are essential to confirm the general existence of large reservoirs of cold molecular halo gas and study them in more detail. Given that the CO in these halo reservoirs may be widespread and is likely not forming stars at the rates seen in high-z star-forming and submm galaxies, we argue that it is important to target the low-J transitions of CO with short-baseline array configurations, and to study samples that are unbiased in IR or submm luminosity.

ACKNOWLEDGEMENTS

A warm thanks to the dedicated staff at the ATCA in Narrabri for their round-the-clock support, with a special thanks to Robin Wark, Warwick Wilson, Jamie Stevens, Phil Edwards and Mark Wieringa for their extra efforts regarding the observing, scheduling and software updates that made this work possible. We also thank Santiago Arribas for useful feedback while drafting this paper and Nina Hatch for her help in trying to retrieve archived data. Thanks to the anonymous referee for suggestions that significantly improved this paper. BE thanks the Centro de Astrobiología (CSIC/INTA) for their hospitality, and CSIRO Astronomy and Space Science for their generosity, during the final stage of this project. The Australia Telescope is funded by the Commonwealth of Australia for operation as a National Facility managed by CSIRO. This

research has made use of the NASA/IPAC Extragalactic Database (NED) which is operated by the Jet Propulsion Laboratory, California Institute of Technology, under contract with the National Aeronautics and Space Administration (NASA). Some of the results presented in this paper were based on observations made with the NASA/ESA *HST*, and obtained from the Hubble Legacy Archive, which is a collaboration between the Space Telescope Science Institute (STScI/NASA), the Space Telescope European Coordinating Facility (ST-ECF/ESA) and the Canadian Astronomy Data Centre (CADC/NRC/CSA). BE acknowledges funding from the Australian Commonwealth Scientific and Industrial Research Organisation (CSIRO) and additional support by the Spanish Ministerio de Economía y Competitividad under grant AYA2010-21161-C02-01. NS is a recipient of an ARC Future Fellowship.

REFERENCES

Alloin D., Barvainis R., Guilloteau S., 2000, ApJ, 528, L81
Aravena M. et al., 2010, ApJ, 718, 177
Aravena M., Wagg J., Papadopoulos P. P., Feain I. J., 2011, ApJ, 737, 64
Aravena M. et al., 2012, MNRAS, 426, 258
Aravena M. et al., 2013, MNRAS, 433, 498
Archibald E. N., Dunlop J. S., Hughes D. H., Rawlings S., Eales S. A., Ivison R. J., 2001, MNRAS, 323, 417
Barthel P. D., Arnaud K. A., 1996, MNRAS, 283, L45
Barthel P., Haas M., Leipski C., Wilkes B., 2012, ApJ, 757, 26
Begelman M. C., Cioffi D. F., 1989, ApJ, 345, L21
Bicknell G. V., Sutherland R. S., van Breugel W. J. M., Dopita M. A., Dey A., Miley G. K., 2000, ApJ, 540, 678
Binette L., Wilman R. J., Villar-Martín M., Fosbury R. A. E., Jarvis M. J., Röttgering H. J. A., 2006, A&A, 459, 31
Blundell K. M., Rawlings S., 2000, AJ, 119, 1111
Blundell K. M., Rawlings S., 2001, ApJ, 562, L5
Bolatto A. D., Wolfire M., Leroy A. K., 2013, ARA&A, 51, 207
Bothwell M. S. et al., 2013, MNRAS, 429, 3047
Briggs D. S., 1995, PhD thesis, New Mexico Institute of Mining and Technology
Carilli C. L., Walter F., 2013, ARA&A, 51, 105
Carilli C. L., Owen F. N., Harris D. E., 1994, AJ, 107, 480
Carilli C. L., Roettgering H. J. A., van Ojik R., Miley G. K., van Breugel W. J. M., 1997, ApJS, 109, 1
Carilli C. L., Harris D. E., Pentericci L., Rottergering H. J. A., Miley G. K., Bremer M. N., 1998, ApJ, 494, L143
Carilli C. L., Harris D. E., Pentericci L., Röttgering H. J. A., Miley G. K., Kurk J. D., van Breugel W., 2002, ApJ, 567, 781
Carilli C. L. et al., 2010, ApJ, 714, 1407
Carilli C. L., Hodge J., Walter F., Riechers D., Daddi E., Dannerbauer H., Morrison G. E., 2011, ApJ, 739, L33
Ceverino D., Dekel A., Bournaud F., 2010, MNRAS, 404, 2151
Chambers K. C., Miley G. K., van Breugel W., 1987, Nature, 329, 604
Chambers K. C., Miley G. K., van Breugel W. J. M., Huang J.-S., 1996, ApJS, 106, 215
Coppin K. E. K. et al., 2008, MNRAS, 389, 45
Coppin K. E. K. et al., 2010, MNRAS, 407, L103
Croft S., Kurk J., van Breugel W., Stanford S. A., de Vries W., Pentericci L., Röttgering H., 2005, AJ, 130, 867
Daddi E., Dannerbauer H., Elbaz D., Dickinson M., Morrison G., Stern D., Ravindranath S., 2008, ApJ, 673, L21
Danielson A. L. R. et al., 2011, MNRAS, 410, 1687
Dannerbauer H., Daddi E., Riechers D. A., Walter F., Carilli C. L., Dickinson M., Elbaz D., Morrison G. E., 2009, ApJ, 698, L178
Dasyra K. M., Combes F., 2012, A&A, 541, L7
De Breuck C., Röttgering H., Miley G., van Breugel W., Best P., 2000, A&A, 362, 519
De Breuck C., Neri R., Omont A., 2003a, New Astron. Rev., 47, 285
De Breuck C. et al., 2003b, A&A, 401, 911
De Breuck C., Downes D., Neri R., van Breugel W., Reuland M., Omont A., Ivison R., 2005, A&A, 430, L1
De Breuck C. et al., 2010, ApJ, 725, 36
De Young D. S., 1989, ApJ, 342, L59
Doherty M. et al., 2010, A&A, 509, A83
Downes D., Solomon P. M., 1998, ApJ, 507, 615
Dunlop J. S., Hughes D. H., Rawlings S., Eales S. A., Ward M. J., 1994, Nature, 370, 347
Edge A. C., 2001, MNRAS, 328, 762
Elbaz D., Jahnke K., Pantin E., Le Borgne D., Letawe G., 2009, A&A, 507, 1359
Emonts B. H. C., Morganti R., Tadhunter C. N., Oosterloo T. A., Holt J., van der Hulst J. M., 2005, MNRAS, 362, 931
Emonts B. H. C. et al., 2011a, MNRAS, 415, 655
Emonts B. H. C. et al., 2011b, ApJ, 734, L25
Emonts B. H. C., Burnett C., Morganti R., Struve C., 2012, MNRAS, 421, 1421
Emonts B. H. C. et al., 2013, MNRAS, 430, 3465
Evans A. S., Sanders D. B., Mazzarella J. M., Solomon P. M., Downes D., Kramer C., Radford S. J. E., 1996, ApJ, 457, 658
Fabian A. C., 1994, ARA&A, 32, 277
Feain I. J., Papadopoulos P. P., Ekers R. D., Middelberg E., 2007, ApJ, 662, 872
Fragile P. C., Murray S. D., Anninos P., van Breugel W., 2004, ApJ, 604, 74
Fu H., Stockton A., 2007a, ApJ, 664, L75
Fu H., Stockton A., 2007b, ApJ, 666, 794
Fu H., Stockton A., 2009, ApJ, 690, 953
Gaibler V., Khochfar S., Krause M., Silk J., 2012, MNRAS, 425, 438
Galametz A., Stern D., De Breuck C., Hatch N., Mayo J., Miley G., Rettura A., Seymour N., Stanford S. A., Vernet J., 2012, ApJ, 749, 169
Galametz A. et al., 2013, A&A, 559, A2
Glover S. C. O., Mac Low M., 2011, MNRAS, 412, 337
Gooch R., 1996, in Jacoby G. H., Barnes J., eds, ASP Conf. Ser. Vol. 101, Astronomical Data Analysis Software and Systems V. Astron. Soc. Pac., San Francisco, p. 80
Greve T. R., Ivison R. J., Papadopoulos P. P., 2004, A&A, 419, 99
Greve T. R. et al., 2005, MNRAS, 359, 1165
Guillard P. et al., 2012, ApJ, 747, 95
Hainline L. J., Blain A. W., Smail I., Alexander D. M., Armus L., Chapman S. C., Ivison R. J., 2011, ApJ, 740, 96
Hatch N. A., Overzier R. A., Kurk J. D., Miley G. K., Röttgering H. J. A., Zirm A. W., 2009, MNRAS, 395, 114
Holt J., Tadhunter C. N., Morganti R., 2008, MNRAS, 387, 639
Humphrey A., Villar-Martín M., Fosbury R., Vernet J., di Serego Alighieri S., 2006, MNRAS, 369, 1103
Humphrey A., Villar-Martín M., Fosbury R., Binette L., Vernet J., De Breuck C., di Serego Alighieri S., 2007, MNRAS, 375, 705
Humphrey A., Villar-Martín M., Vernet J., Fosbury R., di Serego Alighieri S., Binette L., 2008a, MNRAS, 383, 11
Humphrey A. et al., 2008b, MNRAS, 390, 1505
Humphrey A. et al., 2011, MNRAS, 418, 74
Humphrey A., Vernet J., Villar-Martín M., di Serego Alighieri S., Fosbury R. A. E., Cimatti A., 2013, ApJ, 768, L3
Huynh M. T. et al., 2013, MNRAS, 431, L88
Ivison R. J., 1995, MNRAS, 275, L33
Ivison R. J., Dunlop J. S., Smail I., Dey A., Liu M. C., Graham J. R., 2000, ApJ, 542, 27
Ivison R. J. et al., 2008, MNRAS, 390, 1117
Ivison R. J., Papadopoulos P. P., Smail I., Greve T. R., Thomson A. P., Xilouris E. M., Chapman S. C., 2011, MNRAS, 412, 1913
Ivison R. J. et al., 2012, MNRAS, 425, 1320
Jarvis M. J., Wilman R. J., Röttgering H. J. A., Binette L., 2003, MNRAS, 338, 263
Johansson D. et al., 2012, A&A, 543, A62
Kennicutt R. C., Jr, 1998, ApJ, 498, 541
Kirkpatrick C. C., Gitti M., Cavagnolo K. W., McNamara B. R., David L. P., Nulsen P. E. J., Wise M. W., 2009, ApJ, 707, L69

Kirkpatrick C. C., McNamara B. R., Cavagnolo K. W., 2011, ApJ, 731, L23
Klamer I. J., Ekers R. D., Sadler E. M., Hunstead R. W., 2004, ApJ, 612, L97
Klamer I. J., Ekers R. D., Sadler E. M., Weiss A., Hunstead R. W., De Breuck C., 2005, ApJ, 621, L1
Kodama T., Tanaka I., Kajisawa M., Kurk J., Venemans B., De Breuck C., Vernet J., Lidman C., 2007, MNRAS, 377, 1717
Krips M., Neri R., Cox P., 2012, ApJ, 753, 135
Kuiper E. et al., 2011, MNRAS, 415, 2245
Kurk J. D., Pentericci L., Overzier R. A., Röttgering H. J. A., Miley G. K., 2004, A&A, 428, 817
Lacy M., Petric A. O., Martínez-Sansigre A., Ridgway S. E., Sajina A., Urrutia T., Farrah D., 2011, AJ, 142, 196
Large M. I., Mills B. Y., Little A. G., Crawford D. F., Sutton J. M., 1981, MNRAS, 194, 693
Lasker B. M., Sturch C. R., McLean B. J., Russell J. L., Jenkner H., Shara M. M., 1990, AJ, 99, 2019
McCarthy P. J., van Breugel W., Spinrad H., Djorgovski S., 1987, ApJ, 321, L29
McCarthy P. J., Kapahi V. K., van Breugel W., Persson S. E., Athreya R., Subrahmanya C. R., 1996, ApJS, 107, 19
Mahony E. K., Morganti R., Emonts B. H. C., Oosterloo T. A., Tadhunter C., 2013, MNRAS, 435, L58
Massardi M. et al., 2011, MNRAS, 412, 318
Mellema G., Kurk J. D., Röttgering H. J. A., 2002, A&A, 395, L13
Mihos J. C., Hernquist L., 1994, ApJ, 431, L9
Miley G., De Breuck C., 2008, A&AR, 15, 67
Miley G. K. et al., 2006, ApJ, 650, L29
Morganti R., Oosterloo T. A., Emonts B. H. C., van der Hulst J. M., Tadhunter C. N., 2003, ApJ, 593, L69
Morganti R., Oosterloo T. A., Tadhunter C. N., van Moorsel G., Emonts B., 2005, A&A, 439, 521
Morganti R., Holt J., Tadhunter C., Ramos Almeida C., Dicken D., Inskip K., Oosterloo T., Tzioumis T., 2011, A&A, 535, A97
Morganti R., Fogasy J., Paragi Z., Oosterloo T., Orienti M., 2013a, Science, 341, 1082
Morganti R., Frieswijk W., Oonk R. J. B., Oosterloo T., Tadhunter C., 2013b, A&A, 552, L4
Murphy T. et al., 2010, MNRAS, 402, 2403
Nesvadba N. P. H., Lehnert M. D., Eisenhauer F., Gilbert A., Tecza M., Abuter R., 2006, ApJ, 650, 693
Nesvadba N. P. H., Lehnert M. D., De Breuck C., Gilbert A. M., van Breugel W., 2008, A&A, 491, 407
Nesvadba N. P. H. et al., 2009, MNRAS, 395, L16
Nesvadba N. P. H. et al., 2010, A&A, 521, A65
Ogle P., Davies J. E., Appleton P. N., Bertincourt B., Seymour N., Helou G., 2012, ApJ, 751, 13
Overzier R. A., Harris D. E., Carilli C. L., Pentericci L., Röttgering H. J. A., Miley G. K., 2005, A&A, 433, 87
Papadopoulos P. P., Röttgering H. J. A., van der Werf P. P., Guilloteau S., Omont A., van Breugel W. J. M., Tilanus R. P. J., 2000, ApJ, 528, 626
Papadopoulos P., Ivison R., Carilli C., Lewis G., 2001, Nature, 409, 58
Papadopoulos P. P., Greve T. R., Ivison R. J., De Breuck C., 2005, A&A, 444, 813
Papadopoulos P. P., Kovacs A., Evans A. S., Barthel P., 2008a, A&A, 491, 483
Papadopoulos P. P., Feain I. J., Wagg J., Wilner D. J., 2008b, ApJ, 684, 845
Papadopoulos P. P., van der Werf P., Xilouris E., Isaak K. G., Gao Y., 2012, ApJ, 751, 10
Parma P., Murgia M., Morganti R., Capetti A., de Ruiter H. R., Fanti R., 1999, A&A, 344, 7
Pentericci L., Roettgering H. J. A., Miley G. K., Carilli C. L., McCarthy P., 1997, A&A, 326, 580
Pentericci L., Van Reeven W., Carilli C. L., Röttgering H. J. A., Miley G. K., 2000a, A&AS, 145, 121
Pentericci L. et al., 2000b, A&A, 361, L25
Pentericci L., McCarthy P. J., Röttgering H. J. A., Miley G. K., van Breugel W. J. M., Fosbury R., 2001, ApJS, 135, 63
Pentericci L., Kurk J. D., Carilli C. L., Harris D. E., Miley G. K., Röttgering H. J. A., 2002, A&A, 396, 109
Pérez-Torres M.-A., De Breuck C., 2005, MNRAS, 363, L41
Prochaska J. X., Hennawi J. F., 2009, ApJ, 690, 1558
Randall K. E., Hopkins A. M., Norris R. P., Edwards P. G., 2011, MNRAS, 416, 1135
Rawle T. D. et al., 2013, preprint (arXiv:1310.4090)
Rees M. J., 1989, MNRAS, 239, 1p
Riechers D. A. et al., 2011, ApJ, 739, L32
Riechers D. A. et al., 2013, Nature, 496, 329
Rocca-Volmerange B. et al., 2013, MNRAS, 429, 2780
Röttgering H. J. A., Lacy M., Miley G. K., Chambers K. C., Saunders R., 1994, A&AS, 108, 79
Russell J. L., Lasker B. M., Jenkner H., 1988, in Debarbat S., ed., Proc. IAU Symp. 133, Mapping the Sky: Past Heritage and Future Directions. Kluwer, Dordrecht, p. 235
Russell J. L., Lasker B. M., McLean B. J., Sturch C. R., Jenkner H., 1990, AJ, 99, 2059
Sage L. J., 1990, A&A, 239, 125
Salomé P., Combes F., 2003, A&A, 412, 657
Salomé P. et al., 2006, A&A, 454, 437
Salomé P., Combes F., Revaz Y., Downes D., Edge A. C., Fabian A. C., 2011, A&A, 531, A85
Salomé P., Guélin M., Downes D., Cox P., Guilloteau S., Omont A., Gavazzi R., Neri R., 2012, A&A, 545, A57
Sault R. J., Teuben P. J., Wright M. C. H., 1995, in Shaw R. A., Payne H. E., Hayes J. J. E., eds, ASP Conf. Ser. Vol. 77, Astronomical Data Analysis Software and Systems IV. Astron. Soc. Pac., San Francisco, p. 433
Schmidt M., 1959, ApJ, 129, 243
Scoville N. Z., Yun M. S., Windhorst R. A., Keel W. C., Armus L., 1997, ApJ, 485, L21
Seymour N. et al., 2007, ApJS, 171, 353
Seymour N. et al., 2012, ApJ, 755, 146
Smail I., Blundell K., 2013, MNRAS, 434, 3246
Solomon P. M., Barrett J. W., 1991, in Combes F., Casoli F., eds, Proc. IAU Symp. 146, Dynamics of Galaxies and Their Molecular Cloud Distributions. Kluwer, Dordrecht, p. 235
Solomon P. M., Vanden Bout P. A., 2005, ARA&A, 43, 677
Springel V., Frenk C. S., White S. D. M., 2006, Nature, 440, 1137
Stark D. P., Swinbank A. M., Ellis R. S., Dye S., Smail I. R., Richard J., 2008, Nature, 455, 775
Stevens J. A. et al., 2003, Nature, 425, 264
Sutherland R. S., Bicknell G. V., Dopita M. A., 2003, ApJ, 591, 238
Swinbank A. M. et al., 2010, Nature, 464, 733
Tacconi L. J. et al., 2008, ApJ, 680, 246
Tadhunter C. et al., 2011, MNRAS, 412, 960
van Ojik R., Roettgering H. J. A., Miley G. K., Hunstead R. W., 1997a, A&A, 317, 358
van Ojik R. et al., 1997b, A&A, 321, 389
Venemans B. P. et al., 2007, A&A, 461, 823
Vernet J., Fosbury R. A. E., Villar-Martín M., Cohen M. H., Cimatti A., di Serego Alighieri S., Goodrich R. W., 2001, A&A, 366, 7
Villar-Martín M., Vernet J., di Serego Alighieri S., Fosbury R., Pentericci L., Cohen M., Goodrich R., Humphrey A., 2002, MNRAS, 336, 436
Villar-Martín M., Vernet J., di Serego Alighieri S., Fosbury R., Humphrey A., Pentericci L., 2003, MNRAS, 346, 273
Villar-Martín M. et al., 2006, MNRAS, 366, L1
Villar-Martín M., Sánchez S. F., Humphrey A., Dijkstra M., di Serego Alighieri S., De Breuck C., González Delgado R., 2007, MNRAS, 378, 416
Villar-Martín M. et al., 2013, MNRAS, 434, 978
Wang R. et al., 2010, ApJ, 714, 699
Wang R. et al., 2011, ApJ, 739, L34
West M. J., Villumsen J. V., Dekel A., 1991, ApJ, 369, 287
Wilson W. E. et al., 2011, MNRAS, 416, 832

Wylezalek D. et al., 2013, ApJ, 769, 79
Zinn P.-C., Middelberg E., Norris R. P., Dettmar R.-J., 2013, ApJ, 774, 66
Zirm A. W. et al., 2008, ApJ, 680, 224

APPENDIX A: NOTES ON INDIVIDUAL OBJECTS AND THEIR CO(1–0) CONTENT

MRC 0114-211 ($z = 1.40$): MRC 0114-211 has a strong (∼80 mJy) 48 GHz radio continuum flux, and was also detected in the Australia Telescope 20 GHz (AT20G) Survey (Murphy et al. 2010; Massardi et al. 2011). The radio source is a Compact Steep Spectrum object with a total linear extent of 6 kpc (De Breuck et al. 2010; Randall et al. 2011).

We detect CO(1–0) emission 4 arcsec (34 kpc) west of the radio core, along the axis of the compact radio jet (Fig. 5). An archival *HST* image from Programme 8838 (PI: Lehnert) obtained with the Wide-Field Planetary Camera 2 ($WFPC2_{F555W}$) shows faint optical emission centred at the location of the CO(1–0) emission, with brighter emission found just outside the edge of the radio source (Fig. 6). However, since the archival *HST* data were calibrated using the Guide Star Catalogue 1 (GSC-1; Lasker et al. 1990), an astrometric error of ∼1.5 arcsec in these *HST* data is possible (Russell, Lasker & Jenkner 1988; Russell et al. 1990), which could place the bright optical emission at the location of the host galaxy.

As shown in Table 1, the observing time on MRC 0114-211 had to be longer than for the other sources in our sample to reach a similar sensitivity (because observations were done in the lower sensitivity part of the ATCA 7 mm band). In total seven independent runs of 3–5 h on-source observing time each were devoted to this target. Low-level indications for the CO(1–0) signal are present across the individual data sets from these runs.

MRC 0114-211 is the only source in our sample with a large uncertainty in optical redshift ($z = 1.41 \pm 0.05$; McCarthy et al. 1996)

MRC 0152-209 ($z = 1.92$): MRC 0152-209 has an *HST* morphology reminiscent of a major merger system, with large-scale tidal tails and a double nucleus (Pentericci et al. 2001; Emonts et al., in preparation). The 18 kpc-wide radio source is aligned along the main optical emission from the host galaxy (Pentericci et al. 2000a, 2001).

The CO(1–0) detection is discussed in detail in Emonts et al. (2011b). Due to the relatively narrow FWHM ≈400 km s^{-1} of the CO profile, the CO(1–0) peaks at high significance and a high-resolution follow-up study to spatially map the CO emission is in progress (Emonts et al. in preparation; see also Fig. 4).

MRC 0156-252 ($z = 2.02$): MRC 0156-252 contains an extended radio source (diameter 70 kpc; Carilli et al. 1997). Pentericci et al. (2001) showed that there are several companion galaxies detected with *HST*/NICMOS that are aligned along the radio axis, as well as a large reservoir of Lyα emission that stretches inside the extent of the radio source.

The CO(1–0) emission in MRC 0156-209 peaks just outside the bright hotspot of the bent NE radio jet (∼50 kpc or 6 arcsec from the radio core) and aligns with the reservoir of Lyα emission. It is thus feasible that the CO(1–0) and Lyα emission trace the same gas reservoir, which is ionized within the extent of the radio source (possibly through a combination of photoionization of the AGN and shock-excitation by the radio jet; Villar-Martín et al. 2003; Overzier et al. 2005). Just north of the hotspot and region of Lyα and CO(1–0) emission, Overzier et al. (2005) found a tentative reservoir of diffuse X-ray emission. Therefore, an even more complex gas reservoir (with a wide range of temperatures) may surround the bright radio lobe structure.

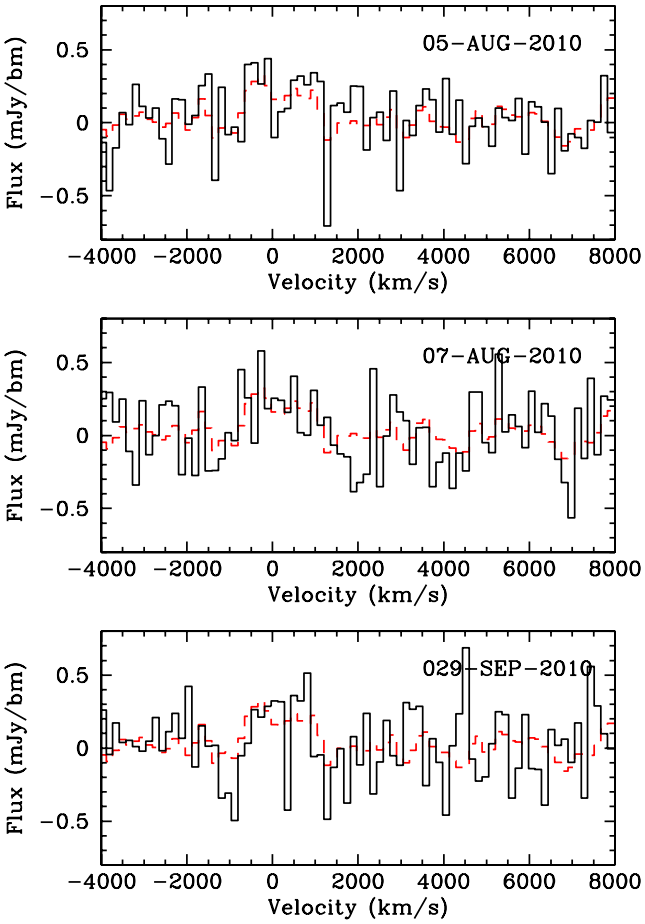

Figure A1. CO(1–0) profiles of MRC 0156-252 taken at the three difference observing epochs (Table 1). The dashed red line is the total spectrum from Fig. 1.

Fig. 7 shows that the CO(1–0) emission appears to consist of two marginally resolved components that are located less than 15–20 kpc from each of the two NE companions in the *HST*/NICMOS image. Recent work by Galametz et al. (2013) suggests that the redshift at which we centred our CO(1–0) profile ($z = 2.016$) is closely related to the redshift of the innermost companion ($z_{\mathrm{He\,II}} = 2.0171 \pm 0.0004$), which has blue colours indicative of star formation (Pentericci et al. 2001, see also Section 3.2.2). According to Galametz et al. (2013), this blue companion is shifted by almost -1000 km s^{-1} with respect to the revised redshift of the central HzRG ($z_{\mathrm{He\,II}} = 2.0256 \pm 0.0002$). The 'blue' and 'red' CO(1–0) component in Fig. 7 have a luminosity of $L'_{\mathrm{CO}} \sim 5 \times 10^{10}$ and $\sim 4 \times 10^{10}$ K km s^{-1} pc^2, respectively.

Because MRC 0156-252 was targeted only during three observing runs, Fig. A1 shows the spectra of the three individual observing epochs. Indications for the signal are present at low-level significance in the data of all three epochs. New observations are in progress to better map the CO(1–0) emission.

MRC 1138-262 ($z = 2.16$): MRC 1138-262, also called the Spiderweb Galaxy, is one of the most massive and active galaxies in the Early Universe (Miley et al. 2006; Seymour et al. 2007;

De Breuck et al. 2010). It is a conglomerate of star-forming galaxies that are embedded in a giant (>200 kpc) Lyα halo, located in the core of the Spiderweb protocluster (Pentericci et al. 1997, 2000b, 2002; Carilli et al. 1998; Kurk et al. 2004; Croft et al. 2005; Kodama et al. 2007; Zirm et al. 2008; Hatch et al. 2009; Doherty et al. 2010; Kuiper et al. 2011). Massive star formation (SFR $\sim 1400\,M_{\odot}\,yr^{-1}$) occurs on scales of >200 kpc (Stevens et al. 2003; Seymour et al. 2007; Ogle et al. 2012). The central galaxy hosts the radio source MRC 1138-262, which induces significant feedback on to the surrounding ISM (Nesvadba et al. 2006; Ogle et al. 2012).

Our CO(1–0) results are discussed in Emonts et al. (2013). Part of the CO(1–0) emission is associated with the central host galaxy of the radio source, but a significant fraction of the gas is spread across at least several tens of kpc (Fig. 3), most likely associated with merging companion galaxies or the IGM between them (see Emonts et al. 2013 for a discussion).

MRC 2048-272 ($z = 2.06$): *HST*/NICMOS and VLA imaging by Pentericci et al. (2000b, 2001) revealed that the radio source is likely hosted by a bright NIR object that is surrounded by two NIR companions. The brighter of the two companions is an AGN (De Breuck et al. 2010). The fainter of the two NIR companions is located in between the tip of the bright NE radio hotspot and the location where the CO(1–0) peaks. Another IR-bright source is located ~8 arcsec SE of the radio galaxy (De Breuck et al. 2010).

For MRC 2048-272, the CO(1–0) profile appears double-peaked and centred around $z_{\mathrm{Ly}\alpha}$ from Venemans et al. (2007). While the overall CO(1–0) emission covers a very wide velocity range (FWZI $= 3570\,km\,s^{-1}$), both peaks are spatially unresolved and centred at the same location, about 56 kpc or 6 arcsec (i.e. one synthesized beam) away from the core of the radio galaxy. For both the blue and red peak, $L'_{\mathrm{CO}} \sim 4 \times 10^{10}\,K\,km\,s^{-1}\,pc^2$. More sensitive observations are required to verify the exact shape of the CO profile and related total CO(1–0) intensity.

This paper has been typeset from a TEX/LATEX file prepared by the author.